Process Safety and Environmental Protection 162 (2022) 775–794

Contents lists available at ScienceDirect

Process Safety and Environmental Protection

journal homepage: www.elsevier.com/locate/psep

Adsorptive properties of MgO/WO_3 nanoadsorbent for selected heavy metals removal from indigenous dyeing wastewater

Chris Agida Uko[a,d], Jimoh Oladejo Tijani[b,d], Saka Ambali Abdulkareem[a,d,e], Saheed Mustapha[b,d,*], Titus Chinedu Egbosiuba[c,d], Edison Muzenda[e]

[a] Department of Chemical Engineering, Federal University of Technology, PMB. 65, Minna, Niger State, Nigeria
[b] Department of Chemistry, Federal University of Technology, PMB, 65, Minna, Niger State, Nigeria
[c] Department of Chemical Engineering, Chukwuemeka Odumegwu Ojukwu University, Uli Campus, Anambra State, Nigeria
[d] Nanotechnology Research Group, Africa Center of Excellence for Mycotoxin and Food Safety, Federal University of Technology, PMB 65, Minna, Niger State, Nigeria
[e] Department of Chemical, Material and Metallurgical Engineering, Botswana International University of Science and Technology, Botswana

ARTICLE INFO

Article history:
Received 14 January 2022
Received in revised form 15 April 2022
Accepted 23 April 2022
Available online 27 April 2022

Keywords:
Tungsten trioxide
Magnesium oxide
Indigenous Dyeing Wastewater
Heavy metals
Adsorption technology

ABSTRACT

The magnesium oxide/tungsten trioxide (MgO/WO_3) nanocomposites were prepared at different mixing ratios using a combination of green and wet impregnation methods and subsequently utilized as nanoadsorbent for the removal of selected heavy metals from Indigenous dyeing wastewater. The synthesized nanomaterials were characterized using High-resolution electron microscopy (HRSEM), High-resolution transmission electron microscopy (HRTEM), Energy Dispersive Spectroscopy (EDS), Selective Area Diffraction (SAED), X-ray diffraction (XRD) and Brunauer Emmett-Teller (BET) N_2 Adsorption-desorption method. HRSEM/HRTEM analysis demonstrated the formation of a distinct spherical shape irrespective of the mixing ratio of MgO on WO_3 nanoparticles. XRD analysis confirmed the existence of a monoclinic phase and face centred cubic phase for WO_3 and MgO nanoparticles and strong interaction between the nanoparticles leading to the formation of magnesium tungstate ($MgWO_4$). The BET analysis revealed a higher surface area (104.2 m^2/g) for mesoporous MgO/WO_3 nanocomposite with a mixing ratio (4:1) than WO_3 alone with a surface area (22.5 m^2/g). The maximum removal efficiency of Cu(II) (98.1%), Fe(II) (100%) and Cr (VI) (100%) was achieved at an optimum contact time of 12, 12 and 14 min respectively. The adsorption data evaluated using Langmuir, Freundlich and Temkin models showed that experimental data best fitted the Langmuir model while the fitness of adsorption data to different kinetic models followed pseudo-second-order. The adsorption of the selected metal ion using MgO/WO_3 nanoadsorbent was based on electrostatic attraction, ion exchange, and pore diffusion mechanism. The thermodynamic study demonstrated the endothermic and spontaneous nature of the metal sorption process. MgO/WO_3 nanoadsorbent with a mixing ratio (4:1) exhibited greater adsorption efficiency than other nanoadsorbents and has excellent regeneration potentials after 5 cycles.

1. Introduction

One of the global problems confronting humanity is water pollution ascribed to the release of untreated wastewater from manufacturing industries; thus, making water bodies unhygienic for the human and aquatic species (Alalwan et al., 2020; Yang et al., 2019; Weerasooriya et al., 2021). The number of manufacturing industries such as indigenous dyeing types has continued to increase due to the increased demand for the dye fabrics and their acceptance among the citizens. The total collapse of the textile industries occasioned by poor managerial skills and inconsistent government policy on small and medium enterprises led to the increase in the indigenous dyeing industries in Nigeria. In addition, the dyeing of fabrics and other clothing materials requires no special skills, unlike the textile industry which needs skilled workers. Indigenous dyeing operation involves mixing plain fabric with different organic dyes for a predetermined period. Not only do the dyes used get fastened to the fabrics but approximately 55% of the dye constituents are discharged as pollutants into the environment (Durotoye et al., 2018). The release of toxic pollutants from indigenous dyeing industries in particular into the

* Corresponding author at: Department of Chemistry, Federal University of Technology, PMB, 65, Minna, Niger State, Nigeria.
E-mail address: saheedmustapha09@gmail.com (S. Mustapha).

https://doi.org/10.1016/j.psep.2022.04.057
0957-5820/

environment has become worrisome due to their toxic nature. The indigenous dyeing wastewater is highly coloured and contained several organic and inorganic pollutants especially heavy metals (Elgarahy et al., 2021; Mishra et al., 2019). However, there is no exact database for the estimated amount of released dyes to the environment because of their huge quantities of pollutants (Kadhom et al., 2020). Heavy metals such as lead (Pb), iron (Fe), chromium (Cr) nickel (Ni), cadmium (Cd) among others present in local dyeing wastewater affects agriculture products and human (Bear et al., 2017). For instance, exposure to Cr(VI) usually causes occupational asthma, eye irritation and damage, perforated eardrums, respiratory irritation, and kidney damage (Ray, 2016). Pb exposure could cause anaemia, weakness, brain damage and even death, especially at high concentrations. Symptoms of exposure to wastewater containing iron include flu-like illnesses such as fever and chills, aches, chest tightness and cough (Obasi and Akudinobi, 2020). Copper (Cu) is an essential element required for good human health, but exposure to a high concentration of Cu is linked to several symptoms such as nausea, vomiting, diarrhea, liver and kidney damage, and even death (Stidworthy and Denk, 2018). In view of the toxic effects of wastewater on fauna and flora, heavy metals like Cu(II), Fe(II) and Cr(VI) in the dyeing wastewater need to be removed before being released into the environment.

Over the past decades, numerous detoxification strategies for the removal of heavy metals from dyeing wastewater which include flotation and sedimentation, ion exchange, chemical precipitation, coagulation, flocculation, electrocoagulation, co-precipitation, filtration, separation membrane, electro-dialysis, photodegradation and adsorption have been explored (Maharana et al., 2021). Among these aforementioned methods, adsorption is an extensive and widely used technique owing to its simplicity, high efficacy, non-secondary pollution, cost-effectiveness and reuse of adsorbent (Karimi-Maleh et al., 2020; Salih et al., 2019, 2020). In the past, different conventional adsorbents such as activated carbon, silica gel, activated alumina have been used for heavy metals removal from wastewater, however, these materials possess low binding sites and the low surface area responsible for their low adsorptive efficiency and in most cases, they are not re-usable.

In recent times, research attention has focused on the application of nanoparticles such as zinc oxide, titanium oxide, nickel oxide, magnesium oxide, tungsten trioxide, cadmium sulphide, cerium oxide, iron oxide and copper oxide as nanoadsorbents for heavy metals removal due to their exceptional properties (Ismail et al., 2019). For instance, WO_3 and MgO nanoparticles are considered non-toxic, environmental friendly, cost-effective, abundant, inexpensive and have antimicrobial activity and excellent photocatalytic/adsorption capacity for heavy metal ions removal from wastewater (Yemmireddy and Hung, 2017). These nanoparticles can be synthesised using physical and chemical methods such as co-precipitation, hydrothermal, vapour deposition, solvothermal, microwave-assisted reduction, photodeposition and photoreduction, chemical vapour deposition, spray pyrolysis, sol-gel and among others (Manjunatha et al., 2020). These synthesis protocols involved complex procedures, long synthesis time, and generation of toxic byproducts (Thiagarajan et al., 2017). Nowadays, green chemistry protocols have been employed to prepare metal oxide nanoparticles due to their simplicity, cost-effectiveness and environmental friendliness. The green synthesis also referred to as biosynthesis involves the mixing of metal salt precursors with either plant extracts or microorganisms (Salem and Fouda, 2021). During this method of reaction, plant extracts act as a stabilizing, capping and reducing agent.

MgO is a multi-functional material with enhanced chemical inertness, optical transparency and high thermal stability and considerable antibacterial properties (Moustafa et al., 2017). Due to its high surface area, it is used as an efficient adsorbent for the removal of numerous toxic chemicals and acids from wastewater (Abinaya et al., 2021; Karthik et al., 2019; Moustafa et al., 2017). Apart from MgO nanoparticles, WO_3 has also attracted significant scientific interest due to its unique chemical, functional, physical properties, the small bandgap energy (2.4–2.8 eV), stable physicochemical properties, and strong photo corrosion stability in aqueous solution as well as stable recyclability potentials (Lai, 2015). However, WO_3 is still far from becoming practical nanoadsorbents applications due to its low surface area. Thus, different strategies such as doping or coupling of WO_3 with other metal oxides have been employed to improve its surface area and adsorptive efficiency. For instance, Jamil et al. (2015) reported the removal of Reactive Black 5 and Reactive Orange 122 from synthetic dye solution using MgO nanoparticles and they found that adsorption equilibrium was attained under the following conditions: contact time of 50 and 70 min, adsorbent dose 0.025 g and 0.03 g, and pH 10 and 2 for Reactive Black 5 and Reactive Orange 122, respectively. Also, Ahmed and Abou-Gamra (2016) reported the adsorptive properties of MgO nanoparticles prepared using a sol-gel method for the removal of fast orange 3 R and bromophenol blue dyes from synthetic dye solution. The authors found that cubic phase MgO nanoparticles have adsorption capacities of 30 and 40 mg/g for the removal of fast orange and bromophenol blue respectively. In the same vein, found that MgO nanoparticles synthesized via the sol-gel method simultaneously inactivated bacteria cells and removed heavy metal ions from the aqueous solution within contact times of 30 and 50 min, respectively. Abshirini et al. (2019) employed MgO/Fe_3O_4 nanocomposite to remove chromium ions from an aqueous solution and they demonstrated that maximum removal efficiency of chromium ions (97.73%) occurred under the following experimental conditions: adsorption dose (1.5 g/L), pH (3), contact time (30 min), reaction temperature (25 °C), initial metal ion concentration (10 mg/L). Mahdavi et al. (2020) studied the removal of phosphorus from water samples using SnO_2 and WO_3 nanoparticles and they found that SnO_2 with a maximum adsorptive capacity of 21.5 mg/g removed more phosphorus (47.2%) than WO_3 nanoparticles with 19.0 mg/g and phosphorus removal efficiency of 45.2% under the following conditions pH (3) and contact time (40 min). Shi et al. (2021) studied the adsorptive behaviour of MgO nanoparticles modified with biochar and revealed maximum removal efficiency of 99.9% for both Pb(II) and Cd(II) using adsorbent dosage (0.02 g), pH (4–7), and equilibrium time 120 and 240 min, respectively.

Despite several research efforts on the adsorptive behaviour of MgO and WO_3 nanomaterials for wastewater treatment, information on the adsorptive potential of the binary nanocomposites of MgO-WO_3 for the treatment of local dyeing wastewater is rare. Herein, this study focused on the preparation of WO_3, MgO and MgO-WO_3 nanoadsorbents using green chemistry protocol and wet impregnation methods. This was followed by the characterizations of the prepared nanomaterials using different analytical tools such as HRSEM, HRTEM, SAED, EDS, XRD, and BET. The adsorptive behaviour of the three nanomaterials for selected heavy metals removal was examined. The experimental data were evaluated using different adsorption isotherms and kinetic models. The reusability potential of the prepared nanoadsorbents was also investigated.

2. Materials and methods

2.1. Materials

The following chemicals/reagents with percentage purity: $Na_2WO_4{\cdot}2H_2O$ (99.6%), HCl (35%), HNO_3 (69.6%), H_2SO_4 (97.8%), NaOH (80%), Na_2CO_3 (98.5%), Na_2SO_4 (99.7%), $Mg(NO_3)_2{\cdot}6H_2O$ (98.0%) were obtained from Sigma Aldrich and used without further purification.

2.2. Collection of plants

Fresh leaves of *Polyathia longifelia* (Masquerade tree), *Green ficus* and *Terminalia catappa* (Satellite tree) were collected from Trade Fare Centre in Chanchaga Local Government Area of Niger state in the North Central region of Nigeria. The leaves were first stripped from their stems, thoroughly washed with de-ionized water and then dried for 5 days under sunlight to remove water content at an estimated average temperature of 32 ± 1.40 °C. The dried samples were then milled into powder using an electric blender and carefully sieved with 2 µm mesh to obtain homogeneous size products.

2.3. Wastewater sample collection and pretreatment

Indigenous dyeing wastewater was collected in a cleaned plastic container from No 23, Chawai Street, Unguwan Sanusi, Kaduna South, Kaduna State in the North-Western region of Nigeria on 21st February 2021. The plastic container was pre-washed with 10% dilute HCl and thoroughly rinsed with de-ionized water before the sample was collected. The wastewater was taken to the laboratory and preserved at 4 °C in the refrigerator. This was to ensure there were no changes in the physicochemical parameters of the wastewater before the batch adsorption study.

2.4. Preparation and quantitative phytochemical screening of plant extracts

Approximately 20.0 g of the powdered plant samples (*Polyathia longifelia, Green ficus* and *Terminalia catappa*) were weighed into separate 500 cm^3 beakers containing 200 cm^3 of distilled water in the ratio of 1:10 (w/v). The mixtures were kept under the continuous stirring condition on a hot plate and stirred for 45 min at 120 rpm and 80 °C. The resultant light brownish mixtures were then allowed to cool at room temperature conditions and then filtered using Whatman No 42 filter paper. The aqueous leave extracts obtained were transferred into already washed plastic bottles and then taken for quantitative phytochemical screening. The quantities of bioactive compounds such as flavonoids, total phenolic contents and tannins present in the selected plant extracts were determined using standard methods described by Roghini and Vijayalakshmi (2017).

2.5. Green synthesis of WO_3 nanoparticles

Sodium tungstate dehydrate, $Na_2WO_4{\cdot}2H_2O$, was used as a precursor salt in the preparation of WO_3 nanoparticles via the biosynthesis route. The choice of *Terminalia catappa* leaves extract over the extracts of *Green ficus* and *Polyathia longifelia* leaves were guided by its higher content of secondary metabolites than others. Thus, approximately 10 cm^3 of aqueous leaf extract of *Terminalia catappa* was added in drops to the solution of 0.12 M $Na_2WO_4{\cdot}2H_2O$ and the mixture was gently heated to 120 °C under continuous stirring at 150 rpm for 30 min. Subsequently, 10% HCl was added in drops to obtain acidic pH (1) considered to be the optimal pH (after attempting pH 3, 4 and 7) due to the maximum yield, stability and extremely higher formation at this pH value. The solution was further stirred for 50 min and allowed to age for 24 h. Thereafter, the yellowish-brown precipitate formed was separated from the aqueous extract, first by decantation and then washed copiously with de-ionized water to remove impurities or residual aqueous extract. To obtain a stable monoclinic form of WO_3 at optimum temperature, the synthesized WO_3 nanoparticles were first crushed into a fine powder using a mortar and pestle and calcined in the furnace at a different temperature ranging from 75 to 550 °C for 3 h. The route to the formation of WO_3 nanoparticles is displayed in Plate I.

2.6. Synthesis of MgO nanoparticles

The synthesis of MgO nanoparticles followed the method reported by Agrawal et al. (2015) with a slight modification. Firstly, 5.21 g (0.2 M) of $Mg(NO_3)_2{\cdot}6H_2O$ was dissolved in 100 cm^3 of de-ionized water in a 500 cm^3 beaker and kept under the continuous stirring condition at 150 rpm and 100 °C for 30 min and a visibly clear solution was obtained. Secondly, 10 cm^3 of aqueous leave extract of *Terminalia catappa* was added to the solution of the precursor salt in drops using a glass rod and the mixture was further stirred for 30 min under the same conditions. Thirdly, a homogenous solution of 8.0 g (2.0 M) NaOH in 100 cm^3 de-ionized water was prepared and the mixture of $Mg(NO_3)_2{\cdot}6H_2O$ and plant extract was added dropwise in beakers using a glass rod until the desired pH of 8, 9, 10 and 11 were achieved. A visible colour change from light yellow to dark yellowish-brown accompanying the formation of precipitates was observed. Finally, the mixtures were further stirred on a magnetic stirrer for 2 h followed by filtration and washing severally with de-ionized water to get the final products. The final products were then kept in a vacuum oven at 80 °C for 4 h to remove moisture and dried product. These dried nanomaterials were first crushed to a fine powder and then calcined at 450 °C for 2 h to obtain the white coloured crystalline MgO nanoparticles. The pictorial representation of the step-by-step synthesis of MgO nanoparticles is shown in Plate II.

2.7. Synthesis of MgO-WO_3 nanocomposite

The wet impregnation method was used for the synthesis of MgO-WO_3 nanocomposite. Firstly, a known mass of as-synthesized WO_3 powder was dispersed in 30 cm^3 of de-ionized water and mixed homogeneously using an ultrasonicator bath operated at room temperature for 30 min. Secondly, known masses of MgO nanoparticles were added to the aforementioned mixture and sonicated for another 30 min to obtain various MgO-WO_3 solutions at the respective ratios of 1:1, 1:2, 2:1, 1:4 and 4:1. The resultant mixtures were poured into a 50 cm^3 Teflon lined autoclave and heated at 120 °C for 3 h. The products obtained were centrifuged, thoroughly washed with de-ionized water, oven-dried at 80 °C for 6 h and finally calcined at 450 °C for 3 h.

2.8. Characterization techniques

The WO_3 nanoparticles, MgO nanoparticles and MgO-WO_3 nanocomposites were characterized using HRTEM for particle size and microstructure analysis, HRSEM for their morphologies, EDS for elemental composition, XRD for the determination of mineralogical phase and BET for their surface-textural properties. The microstructures of the synthesized materials were determined by Zeiss Auriga high-resolution transmission electron microscopy (HRTEM) coupled with energy dispersive spectroscopy (EDS). 0.02 g of the sample was placed in a tube and subjected to ultra-sonication in 10 cm^3 methanol until complete dispersion was obtained. Two drops of the slurry were spread on a holey carbon grid with the aid of a micropipette and subsequently dried by exposure to photo light before analysis. The morphologies of the synthesized samples were investigated using a Zeiss Auriga HRSEM. A mass (0.05 g) of the sample was sprinkled onto carbon adhesives tape and sputter-coated with Au-Pd using a Quorum T15OT for 5 min to enhance the conductivity of the sample. The microscope was operated with electron high tension at 5 kV to examine the image. The samples were characterized with the aid of a Bruker D8 Advance X-ray diffractometer with CuKα radiation to determine their crystal phases and crystallite sizes. The powdered sample was placed on the degreased glass side sample holder and diffractograms were recorded in the 2θ range of 20° to 90°.

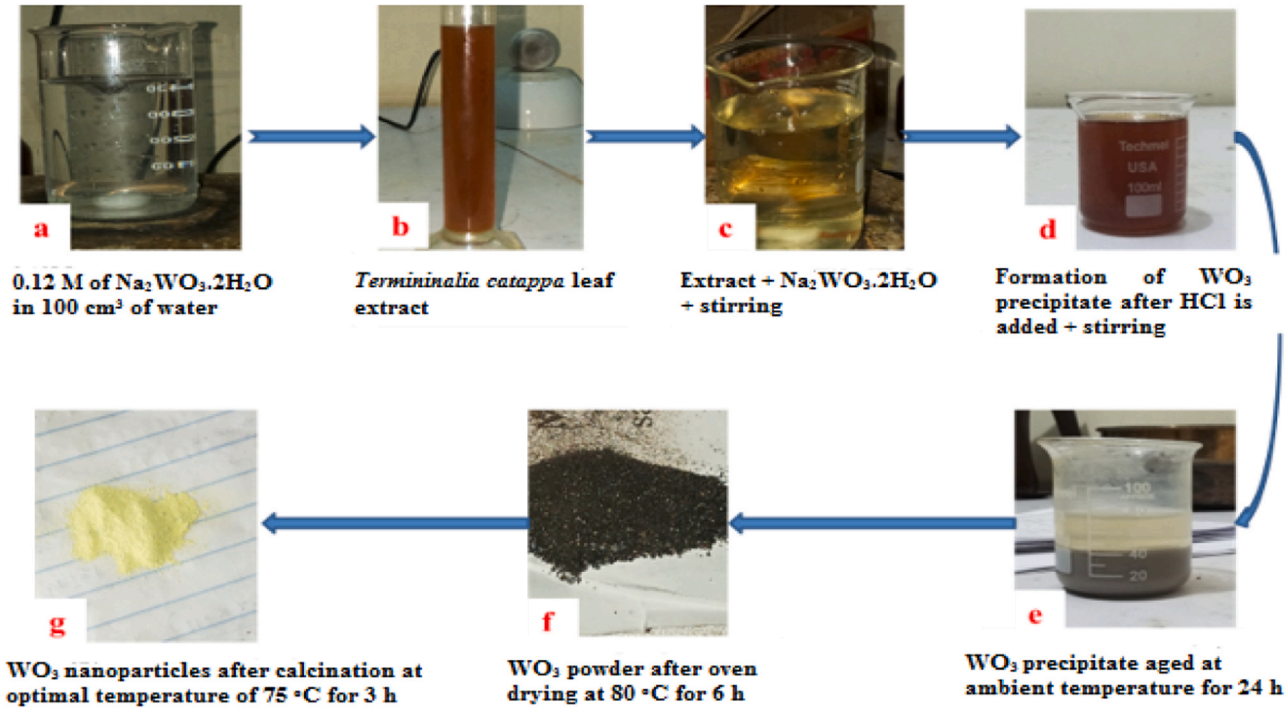

Plate I. Procedure for green synthesis of WO_3 nanoparticles.

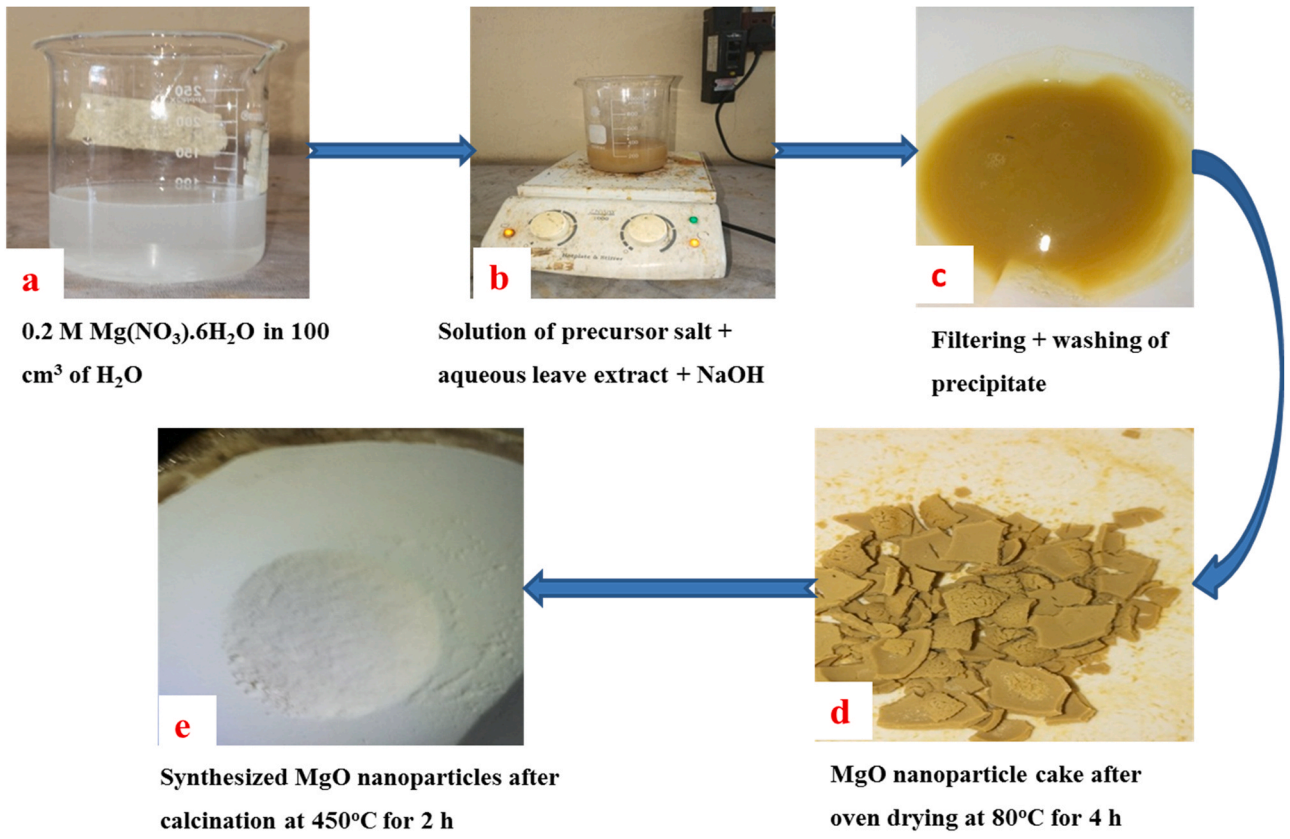

Plate II. Pictorial representation for green synthesis of MgO nanoparticles.

2.9. pHpzc determination

The pHpzc values of MgO, WO_3 and MgO/WO_3 were investigated using the salt addition method. Exactly 40.0 cm^3 of 0.02 M NaCl solution was measured in different beakers and the pH values of the solutions were adjusted to 2, 4, 6, 8, 10 and 12 using 0.02 M HCl and 0.02 M NaOH solutions. The initial pH values were recorded using a pH meter (pH Hanna Instrument Ltd., United Kingdom). A 0.20 g of

each nanoadsorbent was added to each beaker and was shaken using a rotary shaker at 200 rpm for 6 h. The mixtures were allowed to settle and their final pH values were recorded.

2.10. Analysis of wastewater

The water quality parameters were determined before and after treatment of the local dyeing wastewater using the standard methods described by the American Public Health Association (APHA) (2017). The pH was determined with an electric pH meter. Before the pH determination, the pH meter was calibrated with buffers 4, 7 and 11. The TDS and TSS were determined according to the procedure described by APHA (2017). The biochemical oxygen demand (BOD) was determined using the Winkler method. Total organic carbon (TOC) was determined by the TOC analyzer (model, Shimazu 5050 A). Chloride determination was carried out using the Argentometric method. NitraVer 5 Nitrate pillow, sulphate reagent pillow for nitrate, and sulphate respectively were added to each sample cell containing some wastewater and mixed. The phosphate level was determined following the procedure described in APHA (2017). The mixtures were run in the Hach colourimeter, and results were recorded at mg/L. The atomic absorption spectrophotometer (AAS) (Perkin Elmer 200) was used to determine the concentration of the heavy metals in the local dyeing wastewater such as chromium, iron, and copper in wastewater before and after treatment.

2.11. Adsorption experiment

The effects of contact time, adsorbent dosage, and reaction temperature on the removal efficiency of the target metals from wastewater were examined via Batch adsorption mode. The adsorption kinetics, adsorption isotherm and thermodynamic data were analysed. The removal efficiency (% removal) and the adsorption capacity (q_e, mg/g) of some heavy metals in local dyeing wastewater solution using MgO nanoparticles, WO_3 nanoparticles and MgO-WO_3 nanocomposites were determined. The adsorption capacities of the nanoadsorbents were determined as follows:

$$\%\text{removal} = \frac{C_0 - C_e}{C_e} \times 100 \tag{1}$$

$$q_e = \frac{(C_0 - C_e)}{M} V \tag{2}$$

where C_0 (mg/dm^3) and C_e (mg/dm^3) are the initial and equilibrium liquid phase concentration, respectively; V (dm^3) the volume of the solution and M (g) the mass of the adsorbent.

2.11.1. Effect of contact time

The effect of contact time (0–20 min) on adsorption of some heavy metals onto MgO, WO_3 and MgO-WO_3 nanoadsorbents were investigated at a constant pH value of 9.98 of wastewater, initial concentration of metal ions in the wastewater and adsorbent dosage of 0.2 g. The amount of adsorbent dosage (0.2 g) was added to 40 cm^3 of wastewater solution in a corked 250 cm^3 Erlenmeyer flask, agitated on an orbital shaker at the respective time. The solution was filtered using Whatman No 42 filter paper and analyzed for residual concentrations of heavy metals using AAS. The optimum contact time for each metal analyzed was used in this study for the next experiment.

2.11.2. Effect of nanoadsorbent dosage

The effect of nanoadsorbent dosage on the uptake of some heavy metals from wastewater was investigated in adsorbent doses range of 0.2, 0.4, 0.6, 0.8 and 1.0 g. The specified nanoadsorbent doses were added to 40 cm^3 of wastewater solution in a corked 250 cm^3 Erlenmeyer flask, agitated at 150 rpm at the optimum contact time of respective heavy metal while the temperature and pH of the solution remain constant. At the end of the shaking period, the flasks were removed from the orbital shaker and then filtered through Whatman No 42. The filtrates were analyzed for their residual metal ion concentrations using AAS.

2.11.3. Effect of temperature

The effect of reaction temperature on the metal ions uptake from local dyeing wastewater by the nanoadsorbents in the temperatures range of 30, 35, 40, 45, 50, 55 and 60 °C was investigated. The experiments were performed by adding 0.2 g of the nanoadsorbent to 40 cm^3 of dye wastewater in a corked 250 cm^3 Erlenmeyer flask. The resultant mixtures were shaken in a water bath at their respective temperature for the optimum contact time. The residual metal ion concentrations in the wastewater samples were filtered and the filtrates were analyzed using AAS. This procedure was repeated for other temperatures.

2.12. Adsorption isotherm

The adsorption equilibrium isotherms described the interaction between sorbate and sorbent when the amount of solute being adsorbed onto the adsorbent is equal to the amount being desorbed. The Freundlich, Langmuir and Temkin isotherm models are often used to describe the experimental adsorption data.

2.12.1. Langmuir isotherm

Langmuir isotherm assumes the homogeneous adsorption on the surface of the nanoadsorbent. The equation of the isotherm is given by Eq. (3).

$$\frac{C_e}{q_e} = \frac{1}{Q_m K_L} + \frac{1}{Q_m} C_e \tag{3}$$

where C_e is the equilibrium concentration of the pollutants in the solution (mg/dm^3), q_e represents the equilibrium adsorption capacity (mg/g), Q_m is the maximum adsorption capacity (mg/g) and K_L denotes the Langmuir constant that signifies the affinity between adsorbate and adsorbent (L/mg). a plot of $\frac{C_e}{q_e}$ against Ce usually give a straight line with $\frac{1}{Q_m}$ and $\frac{1}{Q_m K_L}$ as slope and intercept respectively.

2.12.2. Freundlich isotherm

Freundlich isotherm represents multilayer adsorption on the adsorbent surface and it is described by Eq. (4).

$$\ln q_e = \frac{1}{n} \ln C_e + \ln K_f \tag{4}$$

where K_f and n are Freundlich constants that are related to adsorption capacity and adsorption intensity, respectively. A plot of $\ln q_e$ against $\ln C_e$ gives a straight-line graph with $\frac{1}{n}$ and $\ln K_f$ as slope and intercepts, respectively.

2.12.3. Temkin isotherm model

The Temkin isotherm model assumes that the heat of sorption decreases with the coverage due to adsorbate-adsorbent interaction and the linearised form is given in Eqs. (5) and (6).

$$q_e = B_T \ln a + B_T \ln C_e \tag{5}$$

$$B_T = \frac{RT}{b_T} \tag{6}$$

A plot of q_e versus ln C_e enables the determination of the isotherm constants a and b_T. a is the Temkin isotherm constant known to be the equilibrium binding constant (L/g) corresponding to the maximum binding energy and b_T (J/mol) is related to the heat of biosorption. The slope and intercept were calculated from the plot of q_e against $\ln C_e$.

2.13. Adsorption kinetic models

2.13.1. Pseudo-first order model

The pseudo-first-order kinetic model assumes that the rate of sorption is proportional to the active adsorbent sites. The equation of Lagergren pseudo-first-order is given by Eq. (7).

$$\ln(q_e - q_t) = \ln q_e - k_1 t \quad (7)$$

where q_e and q_t denote the amount of metals adsorbed (mg/g) at equilibrium and at a time, t, respectively and $k_1$is the rate constant of pseudo-first-order adsorption (min^{-1}).

2.13.2. Pseudo-second order model

The pseudo-second-order assumes that the rate of adsorption sites is proportional to the square of the number of unoccupied adsorbent sites. The pseudo-second-order equation is described by Eq. (8).

$$\frac{t}{q_t} = \frac{1}{k_2 q_e^2} + \frac{t}{q_e} \quad (8)$$

where q_e and q_t are the amount of metals adsorbed at equilibrium and at a time, t, respectively and k_2 is the rate constant of pseudo-second-order adsorption kinetic (g/mg/min).

2.13.3. Intra-particle diffusion model

The basic assumption with the intra-particle diffusion model is that film diffusion is negligible and intraparticle diffusion is the only rate-controlling step. According to Weber and Morris (1963), if the rate-limiting step is the intra-particle diffusion, then the amount adsorbed at any time t should be directly proportional to the square root of contact time, t and shall pass through the origin. This is defined mathematically as shown in Eq. (9).:

$$q_t = K_{id} t^{0.5} + I \quad (9)$$

where q_t (mg/g) is the amount adsorbed at time t (min) and K_{id} (mg/gmin$^{0.5}$) is the intra-particle rate constant. The plot of q_t against t determines the K_{id}.

2.13.4. Thermodynamics studies

The thermodynamic parameters of the adsorption process such as the standard Gibbs free energy $\Delta G^{\ominus}$ (kJ/mol), standard enthalpy $\Delta H^{\ominus}$ (kJ/mol) and entropy $\Delta S^{\ominus}$ (J/molK), were computed from the Vant Hoff equation represented in Eqs. (10) and (11) using the equilibrium adsorption data from temperature studied.

$$\Delta H = -RT\ln K \quad (10)$$

$$\ln K = -\frac{\Delta H}{RT} + \frac{\Delta S}{R} \quad (11)$$

where the slope and intercept of the plot of $\ln K$ versus $\frac{1}{T}$ were used to determine the ΔH and ΔS. R is the gas constants (8.314 J/mol K) and T (K) is the absolute temperature.

2.14. Regeneration study

The reusability potentials of the nanoadsorbents (MgO, WO_3 and MgO-WO_3) were done by treating the used nanoadsorbents with a desorbing agent, 0.5 M HNO_3. The mixture (HNO_3 and adsorbent) in a corked 250 cm^3 Erlenmeyer flask was kept for 30 min in an orbital shaker at 150 rpm and room temperature. The mixture was later dried in an oven at 105 °C. The adsorbed metal ions react with the acid to form their nitrate. The nanoadsorbents were washed severally with de-ionized water until a pH of 7 is attained. Afterwards, the nanoadsorbents were oven-dried at 105 °C for 2 days and further calcined in a furnace at 450 °C for 3 h. The resultant nanoadsorbents were further used in adsorption-desorption cycles. The same adsorbent was re-used for the removal of selected heavy metals in the local dyeing wastewater via batch mode under optimized conditions.

3. Results and discussion

3.1. Qualitative phytochemical screening of Plant Extracts

The results of the quantitative secondary metabolites in the three leave extracts of *Terminalia catappa* (TC), *Polyalthia longifelia* (PL) and *Green ficus* (GF) leaves are displayed in Table S1 of the supplementary information. It was observed that the tannins, flavonoids and total phenolic contents in the plant samples ranged from 8.6 to 9.2 mg/g, 2.7–3.8 mg/g and 4.1–6.9 mg/g, respectively. The abundance of these phytochemical constituents in plant extracts is in the order of TC > GF > PL. From phytochemical analysis results, it was noticed that total phenolic constituents are more than tannins and flavonoids, which suggests that (a phenolic compound) may be responsible for the reduction of metal salts to metal oxide nanoparticles and could also play dual roles as stabilizing and capping agents. This is in agreement with the finding of Asha et al. (2017). Among the plant extract analyzed in this study, TC had the highest phenolic constituents and thus informed the choice of the *Terminalia catappa* extract for the preparation of MgO/WO_3 nanocomposites.

3.2. Characterization of studied nanoadsorbents

3.2.1. XRD analysis

The mineralogical phase and change in structures of WO_3 nanoparticles prepared at calcination temperatures (75, 150, 250, 350, 450 and 550 °C) were determined using the XRD technique and the corresponding pattern is presented in Fig. 1(A). For WO_3 nanoparticles prepared at lower temperatures (75 and 150 °C), low intense diffraction peaks were noticed at 2θ values of 22.7°, 24.3°, 28.2°, 33.6°, 36.6°, 42.9°, 46.5°, 50.0°, 55.5° and 63.5° which correspond to the following crystal planes (001), (110), (200), (111), (201), (300), (002), (220), (221) and (401) The detected peaks were indexed to a pure monoclinic WO_3 with (JCPDS File no. 033–1387) and lattice constants of a = 7.3 Å and c = 3.7 Å respectively. The peaks were broad and overlapping, indicating the small particle size and amorphous nature of WO_3. At 250 °C, the diffraction peaks become sharp, evidence of loss of water molecules and increase crystallinity. All diffraction peaks were assigned to pure monoclinic WO_3 with (JCPDS File no. 033–1387). For WO_3 nanoparticles calcined at 350 °C, a slight shift in the position of the diffraction peaks was observed, different from WO_3 nanoparticles prepared at other temperatures. This suggests phase transformation from monoclinic to an orthorhombic phase of WO_3 with (JCPDS card no. 84–0886). Beyond 350 °C, more intense and sharp diffraction peaks with a narrower full-width at half maximum, which indicate a high degree of crystalline material were observed. No detection of impurities or other peaks at these temperatures is evidence of the formation of the pure monoclinic phase of WO_3. Generally, it was found that the WO_3 preferentially grew along the (001) plane irrespective of the temperatures except for WO_3 prepared at 75 °C and 150 °C. The presence of the dominant crystal network indicates the successful removal of residual water molecules and the formation of more crystalline material. These observations are in agreement with the findings of Nagarjuna et al. (2017) who employed the sol-gel method to prepare nano-crystalline WO_3. The average crystallite sizes of 6.4 ± 0.97 nm, 8.9 ± 1.04 nm, 9 ± 0.80 nm, 13.01 ± 1.09 nm, 15.7 ± 2.15 nm and 17.4 ± 1.90 nm were obtained for WO_3 nanoparticles calcined at 75, 150, 250, 350, 450 and 550 °C, respectively by Debye Scherrer equation shown in Eq. (12).

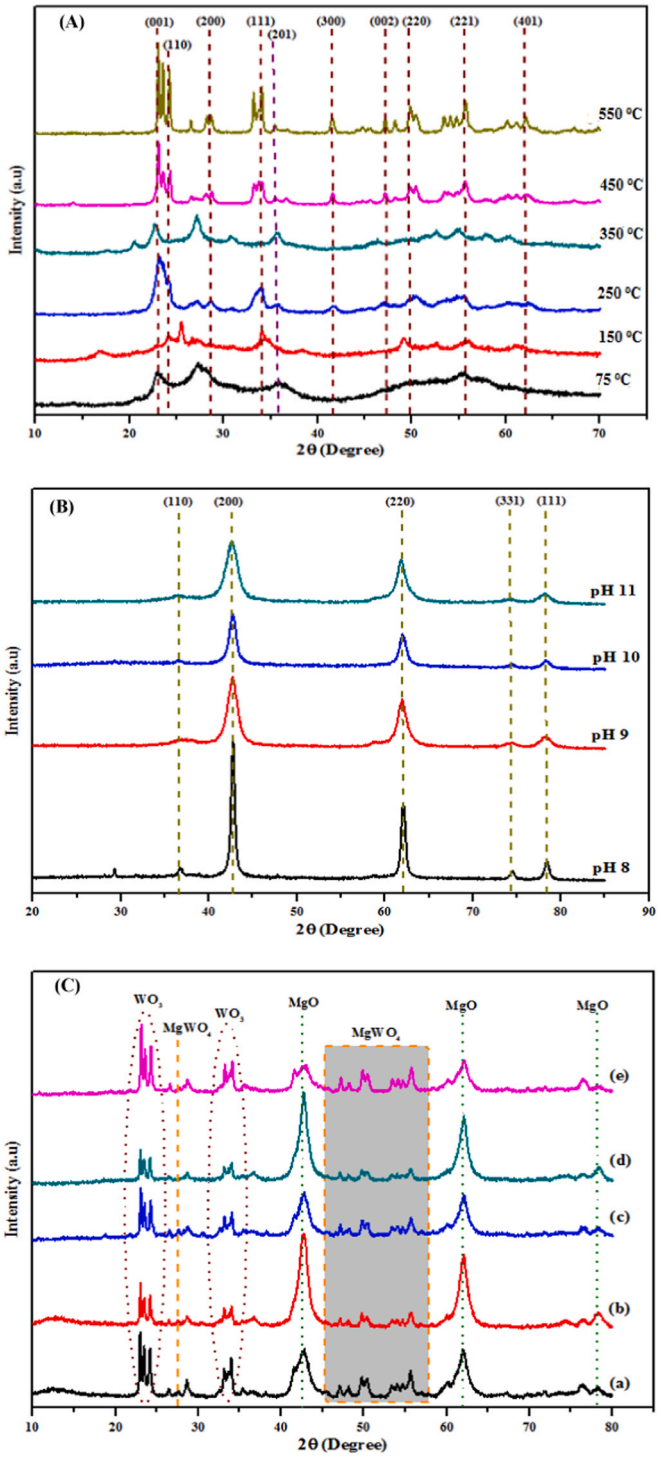

Fig. 1. XRD analysis of (A) WO_3 nanoparticles at different calcination temperature; (B) MgO nanoparticles at different pH values and (C) MgO/WO_3 nanocomposites at different ratios of (a) 1:1 (b) 2:1 (c) 1:2 (d) 4:1 and (e) 1:4.

$$D = \frac{K\lambda}{\beta Cos\theta} \tag{12}$$

where D is the average crystallite size, K is Debye Scherrer's constant (0.94), λ is the Cukα radiation (0.154 nm), β is the full width half maximum (FWHM) of the peak and θ is Bragg's angle.

The increase in the temperature from 75 to 550 °C may be responsible for the increase in the grain size of nanoparticles. The crystal growth along (001) and (201) planes between 250 and 350 °C and a further change in (100), (111) and (300) plane indexes from 450 to 550 °C may be due to inter and intraparticle electrostatic attraction. The observed trend is similar to the findings of Lu et al. (2018) on the effect of sintering temperature on WO_3 prepared using the sol-gel method. They noticed that the average grain size of pure WO_3 calcined at 300, 500 and 700 °C were 235, 343 and 414 nm, respectively, indicating that calcination temperature enhanced its particle size. In this study, particle sizes of WO_3 calcined at different temperatures were found to be lower than the studies of Lu et al. (2018) and Tijani et al. (2019). The plausible reason could be linked to the method of synthesis, type of tungsten precursor and plant extract used as capping and stabilizing agent.

Similarly, the XRD patterns of the prepared MgO nanoparticles at pH 9, 10, 11 and 12 are shown in Fig. 1B. It was noticed that the diffractions peaks at 2θ values of 36.8°, 42.8°, 62.2°, 74.5° and 78.4° correspond to the Miller indices (hkl) (110), (200), (220), (311) and (111) planes that matched with JCPDS Card No. 75–0447. This corresponds to a pure periclase phase of as-synthesized MgO nanoparticles. Non-appearance of the diffraction peaks observed at 2θ values of 29.5° and 37.5° for MgO nanoparticles prepared at pH 9, 10 and 11 may be linked to the presence of more hydroxyl ions in the solution. The excessive amount of hydroxyl ions at these pH values aided the nucleation and growth of MgO nanoparticles compared to pH 8. According to the Debye-Scherrer equation, the average crystallite size of MgO nanoparticles synthesized at pH 9, 10, 11 and 12 was 10.0 ± 2.17 nm, 8.1 ± 1.82 nm, 9.5 ± 1.40 nm and 9.4 ± 1.02 nm, respectively. All of the crystallite sizes obtained in this study were lower than the 20.8 nm reported by Fadil and Kareem (2020). It was noticed that as the pH of the suspended nanoparticles increased, the width of the peaks increased, which suggests the formation of small-sized MgO nanoparticles. The existence of sharp and intense diffraction peaks in the XRD spectrum of MgO irrespective of pH confirmed the formation of crystalline MgO nanoparticles and solution pH did not distort the phase of MgO nanoparticles.

For XRD patterns of as-prepared MgO/WO_3 nanocomposites at different mixing ratios shown in Fig. 1C, it was discovered that diffraction peaks belonging to MgO and WO_3 appeared in the composite samples irrespective of the mixing ratios. Fig. 1C (a-d) revealed the appearance of intense diffraction peaks of MgO at 2θ values of 42.8°, 62.2° and 78.7° that correspond to (200), (220) and (111) planes while the diffraction peaks for WO_3 at 2θ values of 22.7°, 24.5°, 33.6° and 36.6° are related to (001), (110), (111) and (201) planes, respectively. It can be observed from Fig. 1C (e) that peaks belonging to WO_3 nanoparticles were of higher intensity compared to peaks for MgO nanoparticles in the composite sample due to the diffusion effect of Mg (173 pm) onto W (210 pm) based on ionic radius mechanism. The intensities of MgO and WO_3 nanoparticles are mixing ratios dependent. The crystallite size of MgO and WO_3 samples at ratios 1:1, 2:1, 1:2, 4:1 and 1:4 were 13.4 and 15.0 nm, 10.6 and 13.7 nm, 12.5 and 12.9 nm, 9.5 and 11.4 nm and 15.1 and 13.0 nm, respectively. All the XRD patterns of MgO/WO_3 nanocomposite samples revealed the occurrence of diffraction peaks assigned to $MgWO_4$, suggesting strong chemical reactions between MgO and WO_3. The formation of $MgWO_4$ can be explained by Eqs. (13) – (16).

$$Na_2WO_4.2H_2O + 2HCl \rightarrow H_2WO_4.2H_2O + 2NaCl \tag{13}$$

$$H_2WO_4 2H_2O \rightarrow WO_3 + 6H_2O \tag{14}$$

$$2Mg(NO_3)_2.6H_2O \rightarrow 2MgO + 4NO_2 + O_2 + 12H_2O \tag{15}$$

$$WO_3 + MgO \rightarrow MgWO_4 \tag{16}$$

3.2.2. HRSEM/EDX analysis

The morphology of WO_3 nanoparticles calcined at 75, 150, 250, 350, 450 and 550 °C was investigated using HRSEM and the corresponding micrographs are shown in Fig. 2. HRSEM images of WO_3

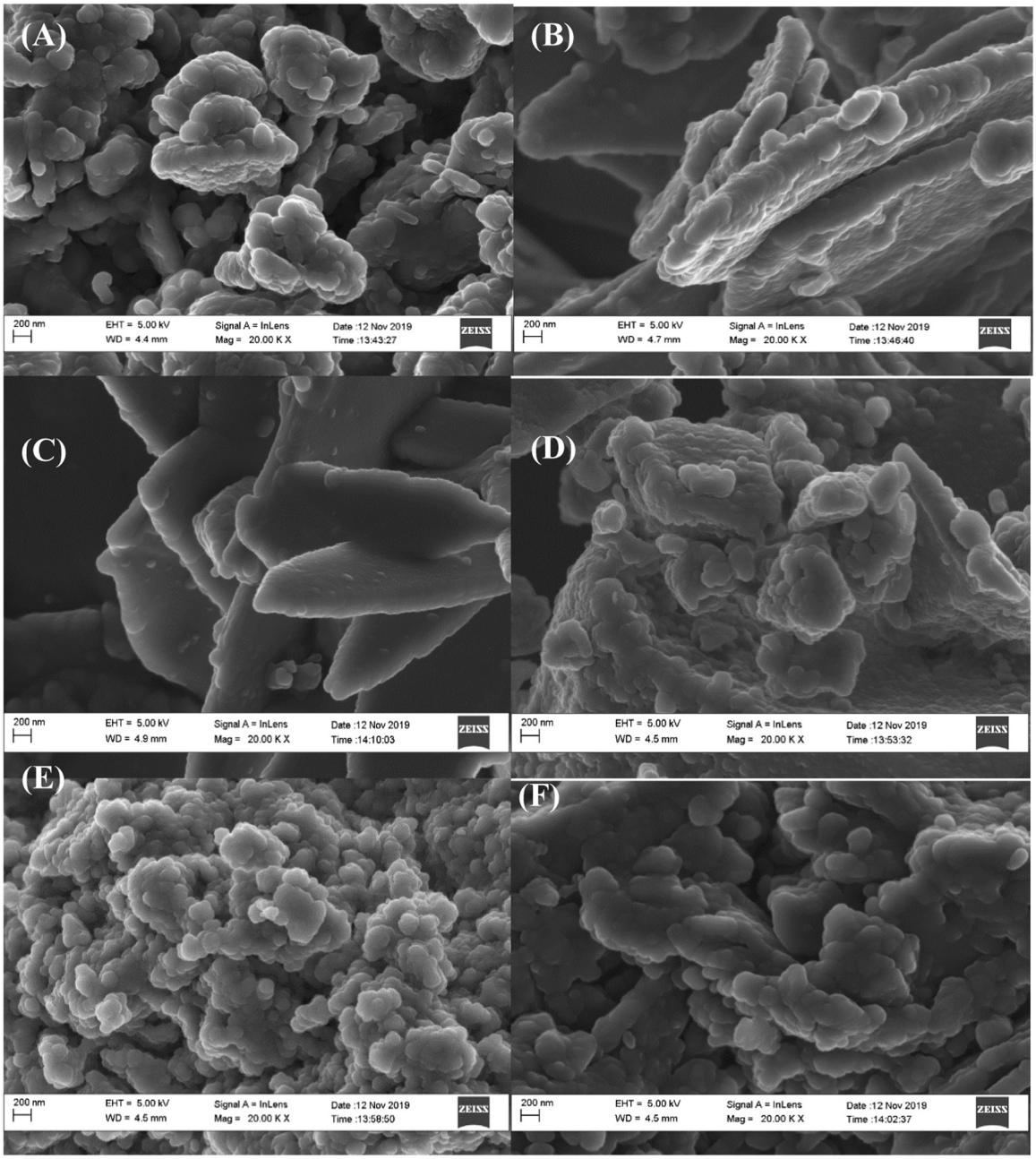

Fig. 2. HRSEM images of WO_3 nanoparticles calcined at (A) 75 °C (B) 150 °C (C) 250 °C (D) 350 °C (E) 450 °C and (F) 550 °C).

calcined at 75, 350, 450 and 550 °C showed the appearance of discrete particles compared to HRSEM images of WO_3 nanoparticles calcined at 150 and 250 °C. The calcination temperatures of 150, 250 and 350 °C, WO_3 nanoparticles exhibited racemose structure with size particles ranging between 200 and 3000 nm while HRSEM images of the synthesized WO_3 nanoparticles at 75, 450 and 550 °C depict the agglomerated spherical structure of size 12.1 ± 0.90 nm, 23.4 ± 1.42 nm and 24.1 ± 1.60 nm, respectively. This shows that particle sizes increase with increasing calcination temperatures. At higher temperatures, agglomerated spherical shaped nanoparticles exhibited conventional Ostwald ripening and oriented attachment mechanism (Jamali and Tehran 2020).

EDX was used to examine the elemental compositions of WO_3 nanoparticles and their atomic percentage is indicated in Fig. S1. EDX analysis demonstrated the presence of W and O elements with W as the major element in the WO_3 nanoparticles prepared at 75, 150 and 250 °C. At high calcination temperature above 250 °C, it was observed that the solid-state reaction between the mono-oxide nanoparticles phase became reduced in W while O content increased, thus this could be linked to the diffusional effect of W (0.062 nm) into O (0.14 nm) at the inner and outer shell of nanoparticles.

The HRSEM was used to investigate the surface morphologies of MgO nanoparticles synthesized at pH 9, 10, 11 and 12 and their corresponding images are shown in Fig. 3. It was observed that the as-synthesized nanoparticles compose of a well-distributed spherical shape. MgO nanoparticles prepared at pH 11 exhibited spherical particle-like shapes with a porous network coupled with less agglomeration. This agglomeration could be due to attractive forces between the phytochemical constituents in the plant extracts and magnesium salt precursor. The MgO nanoparticles prepared in a basic medium exhibited a negative surface charge based on the interactions between the hydroxyl ions in the solutions and the

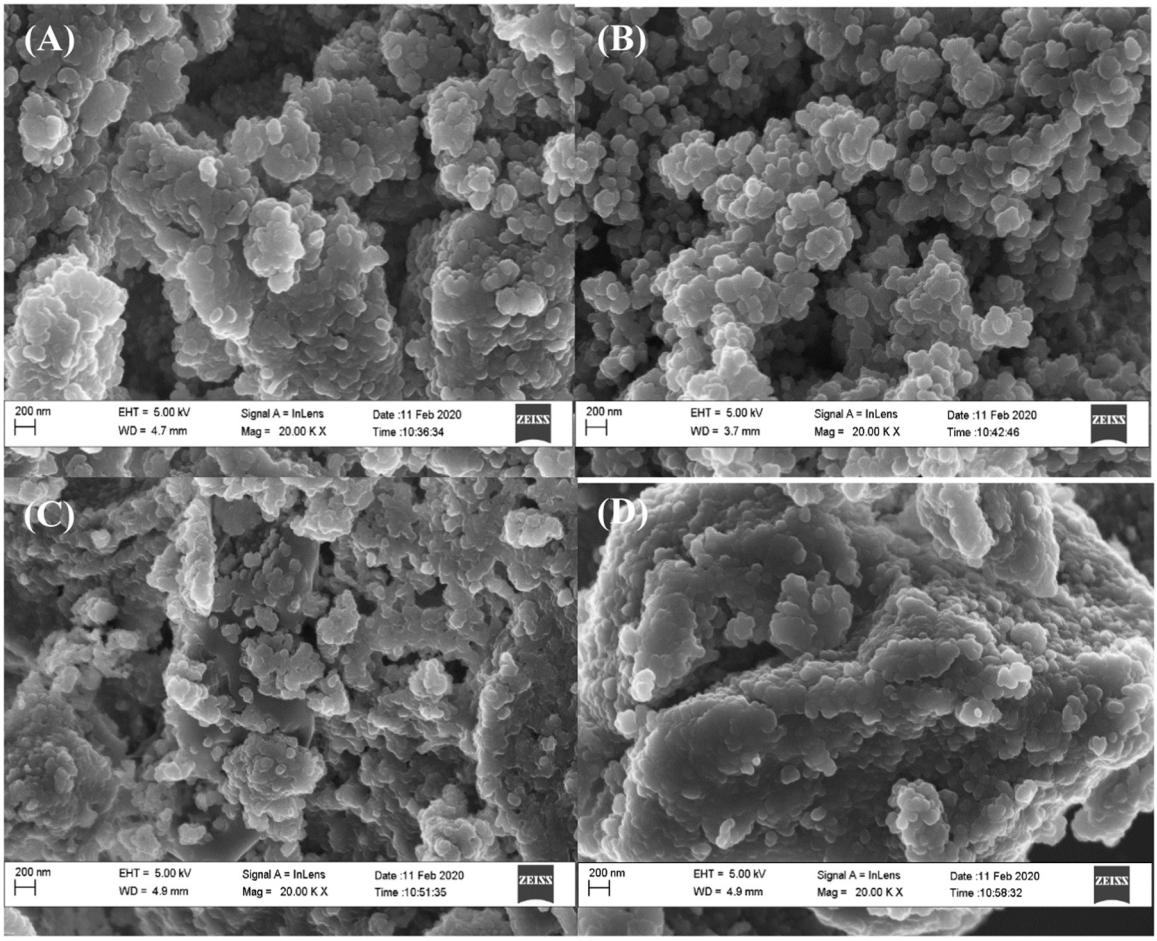

Fig. 3. HRSEM results of synthesized MgO nanoparticles at (A) pH 8 (B) pH 9 (C) pH 10 (D) pH 11 for 450 °C.

positive charges on the meta; surface material (Cai et al., 2017). As a result, the hydroxyl ions give rise to the nucleation, growth and formation of MgO nanoparticles. The morphologies of the MgO nanoparticles at pH 8, 9, 10 and 11 show particles of average sizes 15.9 ± 1.51, 14.5 ± 1.38 nm, 11.9 ± 1.41 and 9.3 ± 1.10 nm, respectively, with a slight degree of agglomeration.

The EDX spectra revealed the presence of Mg, Cl, Na and O in MgO nanoparticles prepared at pH 8, 9 and 10 except for pH 11 as presented in Fig. S2. The Na emanated from the precipitating agent (NaOH) and was not removed due to incomplete washing. EDX result shows that as-synthesized MgO nanoparticles at pH 11 are composed of Mg and O, indicating that the nanoparticles are pure MgO nanoparticles.

Fig. 4 presents the HRSEM images of as-synthesized MgO/WO_3 nanocomposites at different mixing ratios of MgO and WO_3. The MgO nanoparticles were agglomerated in the composite samples except for MgO/WO_3 at 4:1 (as seen in Fig. 4D) which exhibited a flake-like morphology. It was noticed that the shape and size of MgO/WO_3 nanocomposites depend on the composition ratios. This can be linked to the displacement effect of O in Mg by W in WO_3 to form WO_4. The ionic radius of Mg (0.072 nm) is lower than that of O (0.14 nm); thus, Mg can easily diffuse onto the inner pore of W by displacing O with a greater ionic radius.

Elemental distributions of the nanocomposites were examined using EDX and the results are depicted in Fig. S3. The EDX results show the presence of three elements namely; Mg, W and O in all MgO/WO_3 nanocomposites. All the samples exhibited different atomic percentages due to the proportional mixture of MgO and WO_3 nanoparticles in the materials. The nanocomposites did not indicate any other elements in the spectrum, suggesting strong interaction between pure MgO and WO_3.

3.3. HRTEM analysis

Fig. 5 shows low and high magnification HRTEM images of MgO/WO_3 nanocomposites prepared at different ratios with their corresponding SAED patterns. The nanocomposites exhibited uneven surface distribution of the mixed nanoparticles and this could be attributed to the different mixing ratios of the nanoparticles. Fig. 5 (D and J) demonstrated the flake-like structure of MgO/WO_3 composites. The flake-like structure covered the surface of the image, also forming an interface between the WO_3 flake-like structure and the MgO layer. In contrast, Fig. 5 (A, G and M) revealed dark spots and spherical nanoscale bumps on the surface of the nanocomposites.

In Fig. 5 (M), the growth of WO_3 nanostructures onto the surface of the MgO nanoparticles was homogenous irrespective of the MgO to WO_3 ratio. This study corresponds to the finding of Zhang et al. (2017) on the formation of Cr_2O_3/WO_3 nanostructure. They inferred that MgO nanoparticles appeared on the surface of WO_3 nanostructures and the surface of WO_3 surface also synchronously increase with increasing atom (W/Cr) at WO_3/Cr_2O_3 nanocomposites 10:1. The lattice spacing of MgO and WO_3 nanostructures are represented in Fig. 5 (J, K, M and N). Notably, lattice fringes of 0.36 nm which correspond to the (200) plane of WO_3 and 0.25 nm for (111) crystallographic plane of MgO dominated in Fig. 5 (J, K, M and N), respectively. This corroborated the XRD results. Similarly, Lei et al. (2018) noticed that after impregnation of ZnO on the surface of WO_3

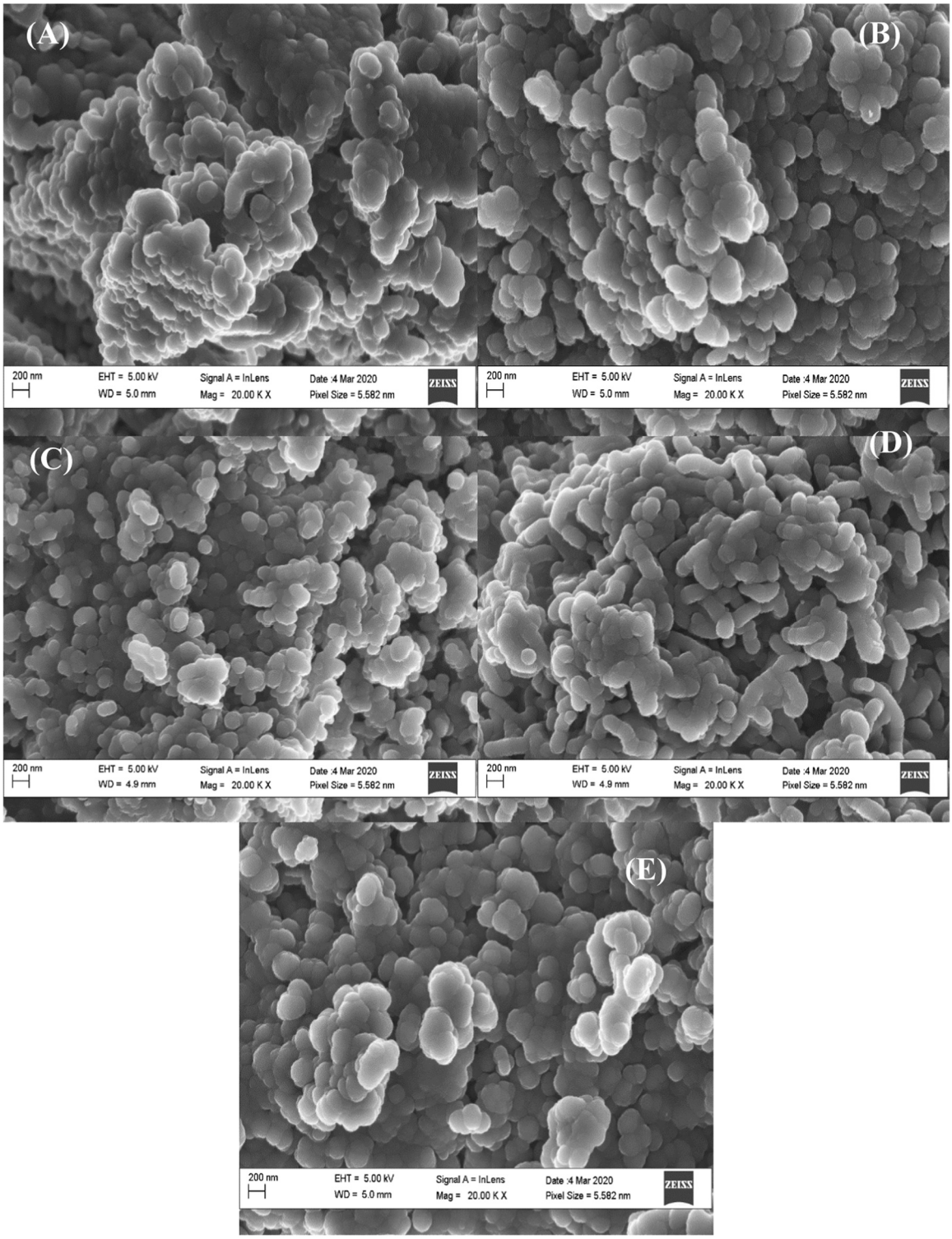

Fig. 4. HRSEM results of synthesized MgO/WO_3 nanocomposites at (A) 1:1 (B) 2:1 (C) 1:2 (D) 4:1 and (E) 1:4.

nanoparticles, the crystallographic orientation and lattice spacing of the WO_3 nanoparticles changed. The corresponding SAED patterns shown in Fig. 5 (C, F, I, L and O) with their concentric ring patterns indicate the polycrystalline nature of the MgO/WO_3 structure. Furthermore, the diffraction rings were clear and sharp in Fig. 5 (F and I), indicating the crystalline grains are tiny in Fig. 5 (F) and evenly scattered in Fig. 5 (O). The EDX results indicated that the as-prepared nanocomposites were composed of O, Mg and W (Fig. S3). This confirmed the pure formation of oxide of Mg and W. The atomic ratios of Mg and W in the EDX results varied depending on the mixing components (MgO and WO_3).

3.4. BET analysis of MgO/WO_3 nanocomposite

The BET analysis of the prepared nanocomposites was carried out to determine its surface area and pore size distribution pattern. The results of the N_2 adsorption-desorption isotherm of WO_3, MgO, and MgO/WO_3 nanocomposites prepared at ratios 1:1, 2:1, 1:2, 1:4 and

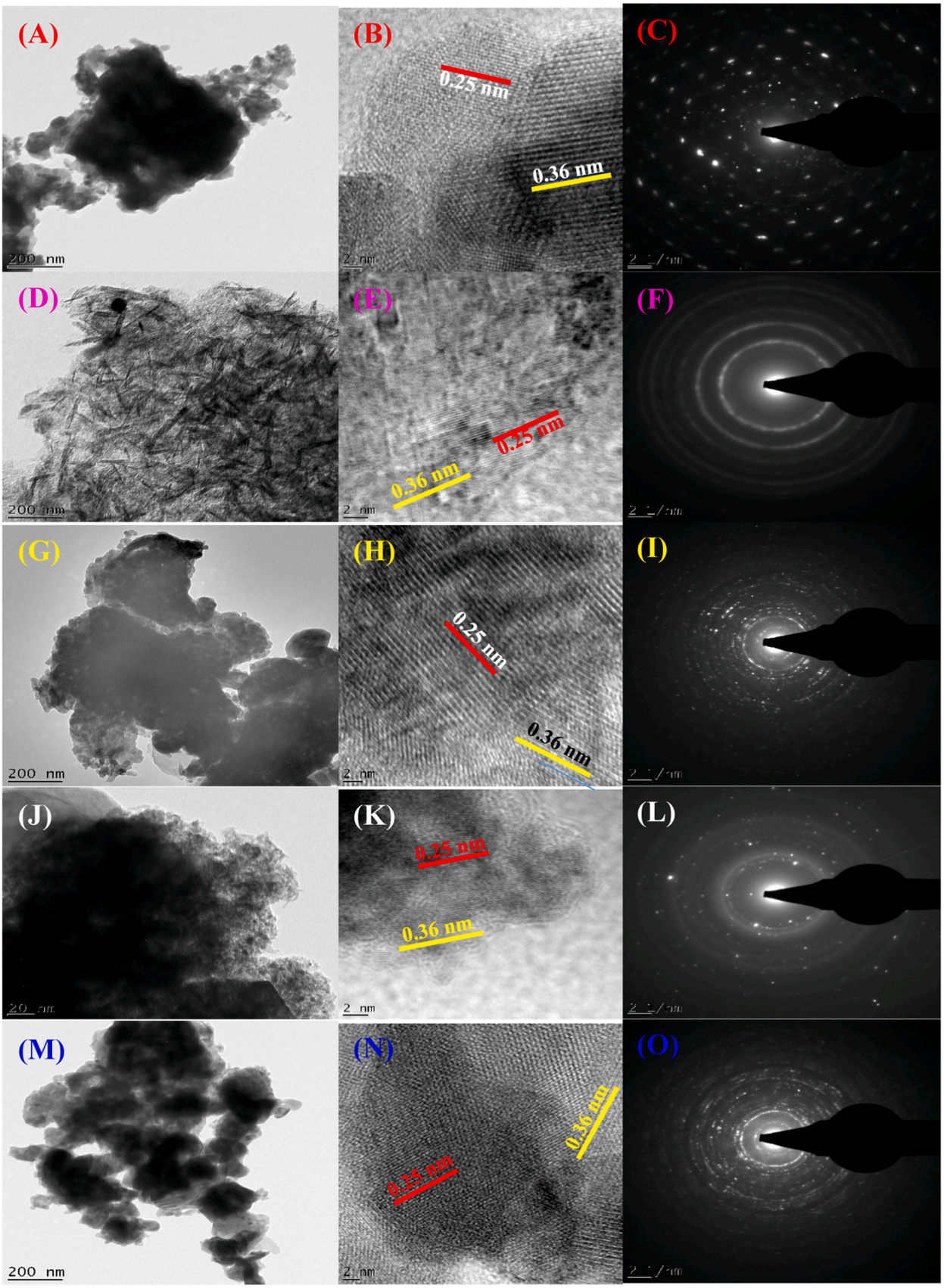

Fig. 5. HRTEM images (high and low) magnification and SAED patterns of MgO/WO_3 at different mixing ratios (A-C) 1:1; (D-F) 1:2; (G-I) 2:1; (J-L) 4:1 and (M-O) 1:4.

4:1 are presented in Table S2. The specific surface areas of the WO_3 and MgO/WO_3 nanocomposites prepared at 1:1, 1:2, 2:1, 1:4 and 4:1 mixing ratios were 22.5, 30.0, 33.6, 45.3, 42.4 and 104.2 m^2/g, respectively. From Table S2, it was found that the BET specific surface area according to the Barrette-Joyner-Halenda (BJH) method increased due to the addition of MgO nanoparticles. This shows that the addition of MgO widens the inner and outer pores of WO_3 nanoparticles, thus responsible for its higher surface area. The four nanocomposites were categorized as mesoporous material because the pore sizes were greater than 2 nm but less than 50 nm. It was observed that the pore volume of MgO/WO_3 nanocomposite samples reduced despite the increase in surface area of the nanocomposites with mixing ratios of 1:4 (0.071 cc/g) and 4:1 (0.054 cc/g). The specific surface area of MgO/WO_3 nanocomposites with a mixing ratio (4:1) in this study was higher than the specific area of MgO/Fe_3O_4 nanocomposite of 75.21 m^2/g reported by Abshirini et al. (2019). The difference in the surface area could be linked to the amount of nanoparticles mixing ratio, nature of added metal oxide, and calcination temperature with respect to the time used in this study. The pore size distributions of nanocomposites at 1:1, 2:1, 1:2, 1:4 and 4:1 was 2.2, 2.1, 2.1, 2.1 and 2.1 nm, respectively. The reduction in the pore sizes with an increase in MgO and WO_3 nanoparticles in the mixing validates the successful incorporation of these nanoparticles in the samples. The MgO/WO_3 nanocomposites (4:1) with the highest surface area could rapidly adsorb pollutants more than others.

3.5. Point of zero charge

The point of zero charge (pzc) of MgO, WO_3 and MgO/WO_3 nanocomposites was determined and the result is depicted in Fig. 6. The pzc of MgO, WO_3 and MgO/WO_3 was found to be 9.74, 2.71 and 8.77, respectively. Based on the pzc value of MgO, the material exhibited alkaline behaviour in the aqueous solution while WO_3 nanoparticles was acidic in nature. The pzc for WO_3 in this study was slightly higher than the 2.49 reported by Thwala et al. (2019). This may be due to the differences in the methods of WO_3 preparation. On the other hand, a shift in pzc was observed for MgO/WO_3 due to the replacement of the W^{6+} with Mg^{2+} which influence the overall charges of the nanocomposite. Furthermore, a shift in pzc to higher pH values was linked to the bounding of hydroxyl ions to the oxide surface which made the surface becomes more positive.

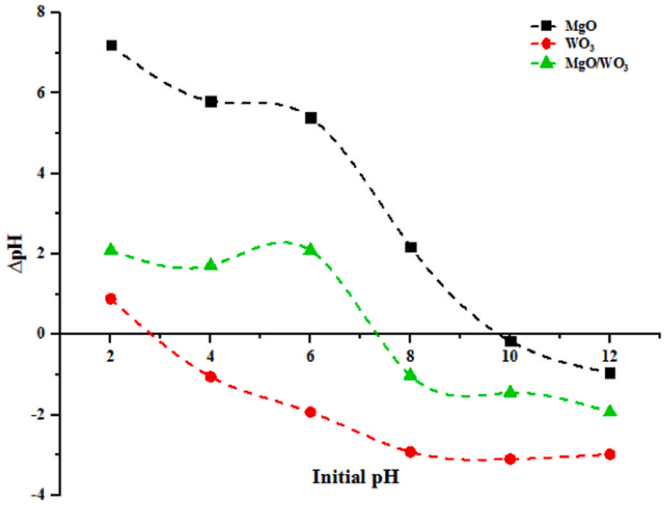

Fig. 6. Point of zero charges of MgO, WO_3 and MgO/WO_3 nanoadsorbents.

3.6. Physicochemical properties of local dyeing wastewater

The results of the physicochemical analysis of Indigenous dyeing wastewater are shown in Table 1. It was noticed that the pH value of the wastewater is high and this may increase the chance of solubilization of main essential elements if released into natural water bodies. In Table 1, the pH value was found to be 9.98, which implies that the wastewater is alkaline due to the presence of scouring and bleaching agents like chemicals such as sodium hypochlorite, sodium hydroxide, surfactants and sodium phosphate used during mercerizing of the fabric. The pH influences plant growth, survival of aquatic animals and activity of useful microorganisms (Naik et al., 2019). This parameter alters the soil permeability which results from underground water contamination. Colour is one of the major problems associated with local dyeing wastewater and the colour of the collected wastewater was blue due to the presence of dissolved salts as shown in Table 1. The UV–visible spectroscopic analysis measured at a wavelength of 625 nm indicated the presence of Remazol Brilliant Blue R (RBBR) in the wastewater (see Fig. S4).

TDS measures the total organic and inorganic substances in the water which include soluble salts (Simeon et al., 2019). These dissolved salts in water cause skin dehydration in animals and give a laxative effect and unpleasant mineral taste to water. TDS increases the osmotic pressure of soil water leading to an increase in respiration rate and a reduction in the growth and yield of most plants (Hafez et al., 2020). The wastewater showed a high level of TDS (1845.6 mg/dm^3) as presented in Table 1 due to the discharge of chemical agents used in various stages of the local dyeing operation. TSS indicates the organic and mineral particles in wastewater that comprises carbonates, bicarbonates, chlorides and phosphates (Chockalingam et al., 2019). The values of TSS value in the wastewater was 504.9 mg/dm^3. The concentration of TSS often influences sedimentation rate and turbidity in the wastewater and increases the oxygen demand, pathogens and contaminants. The chloride in dyeing wastewater has been linked to hydrochloric acid and chlorine gas used during bleaching, washing and disinfection processes during the dyeing processes. The level of chloride was 6508.3 mg/dm^3 in the wastewater and this level could affect crops, microorganisms in water, and increases corrosiveness with resultant adverse health effects on humans. The high amount of chloride influences the level of electrical conductivity, alkalinity, TSS, TDS and

Table 1
Physicochemical properties of local dyeing wastewater.

Parameter	Recorded value	WHO, (2007)	NIS, (2007)
Colour	Blue		
Odour	Objectionable		
pH	9.98 ± 0.19	5–5.9	6.5–8.5
Chemical oxygen demand (COD) (mg/dm^3)	2016.80 ± 0.45	250	60
Biological oxygen demand (BOD) (mg/dm^3)	750.20 ± 0.80	30	30
Electrical conductivity (μS/cm)	1809.20 ± 0.80	1200	1000
Chloride (mg/dm^3)	6508.30 ± 1.20	1000	250
Nitrate (mg/dm^3)	98.60 ± 0.30		
Sulphate (mg/dm^3)	2067.80 ± 0.70		
Total suspended solids (TSS) (mg/dm^3)	504.90 ± 0.80	60	150
Total dissolved solids (TDS) (mg/dm^3)	1845.60 ± 0.23		500
Nitrite (mg/dm^3)	46.50 ± 1.60	3	0.5
Total organic carbon (TOC) (%)	2.15 ± 1.02		
Copper (mg/dm^3)	6.03 ± 0.48	0.1	1.0
Chromium (mg/dm^3)	8.15 ± 0.31	2	0.05
Iron (mg/dm^3)	5.95 ± 0.20	0.3	0.01

Key: WHO (World Health Organization, 2007); NIS (Nigerian Industrial Standard, 2007)

sulphate in wastewater. High levels of chlorides, nitrates and sulphates above the tolerable limits pose a serious threat to aquatic life.

TOC was 2.2 mg/dm^3 in the dyeing wastewater as seen in Table 1. This pollutant measures the amount of organic substances in the wastewater sample. The quantity of the demand for oxygen of oxidizable pollutants in wastewater is described as COD. This parameter shows the level of toxicity and the presence of biological resistant substances in water. According to Table 1, the amount of COD in the wastewater sample was 2016.80 mg/dm^3 which was above the tolerable limits of WHO, (2007) and NIS, (2007). The high value of COD in this study indicates the toxic nature of the wastewater ascribed to the presence of non-biodegradable dyeing chemicals, softeners and detergents (both organic and inorganic constituents) used during the dyeing process (Pensupa et al., 2017). The BOD measures the quantity of oxygen required by bacteria in the wastewater to break down the organic matter present. The dyeing wastewater sample collected showed a BOD value of 750.20 mg/dm^3 as seen in Table 1. In this study, the recorded value of BOD was higher than the WHO, (2007) and NIS, (2007) standards. The high values of BOD indicate the water pollution strength, leading to less availability of oxygen for the living organisms in the wastewater and an increase in the anaerobic properties of wastewater. Higher BOD values also suggest the presence of higher organic impurities samples from dye wastewater. The electrical conductivity (EC) of the wastewater was higher compared to the acceptable limits and wastewater very rich in EC could negatively impact both aquatic and terrestrial species. According to Table 1, the concentrations of the selected heavy metal ions in the collected wastewater are significantly above the permissible limits of WHO and NIS. The order of the abundance of the metal ions is Cr > Cu > Fe. Cr was the most predominant and exposure to wastewater containing high amounts of chromium could result in malfunctioning kidneys and liver. While the low dosage of Cr helps in lipid and protein metabolism as well as maintenance of glucose tolerance factors. Cu was the second most abundant metal in the dyeing wastewater and was noticed to be above the tolerable limits. A high concentration of Cu often prevents the uptake of iron and seed germination while at low concentrations, Cu promotes soil fertility (Yaseen and Scholz, 2019). The toxicity of Cu to aquatic life is a function of the alkalinity of the aquatic environment and copper becomes highly toxic at lower alkalinity (Reddy and Jabez Osborne, 2020). Fe is one of the metals with significant environmental challenges and the concentration of Fe in the dyeing wastewater is twenty times higher than the permissible limits. Exposure to a high concentration of Fe often leads to diabetes, stomach disorder, nausea and even causes damage to the heart. Higher pH values together with heavy metals loads increase the toxicity of the wastewater, thus, the wastewater needs to be treated to support the survival of water living organisms.

3.7. Adsorption studies

3.7.1. Effect of contact time

Contact time is one of the essential factors used to determine the extent of the adsorption process as it establishes the plateau time for the sorbent-sorbate system. Therefore, the determination of optimum contact time signifies the removal efficiency of sorbent in the sequestration of pollutants in dyeing wastewater. The influence of the contact time on the adsorption behaviour of MgO, WO_3 and MgO/WO_3 nanoadsorbents for the removal of selected heavy metals from dyeing wastewater was investigated and varied between 0 and 20 min and the result obtained is depicted in Fig. 7 (A-C). As shown in Fig. 7 (A-C), it can be noticed that the removal efficiencies of the selected heavy metal ions rapidly increased till the equilibrium

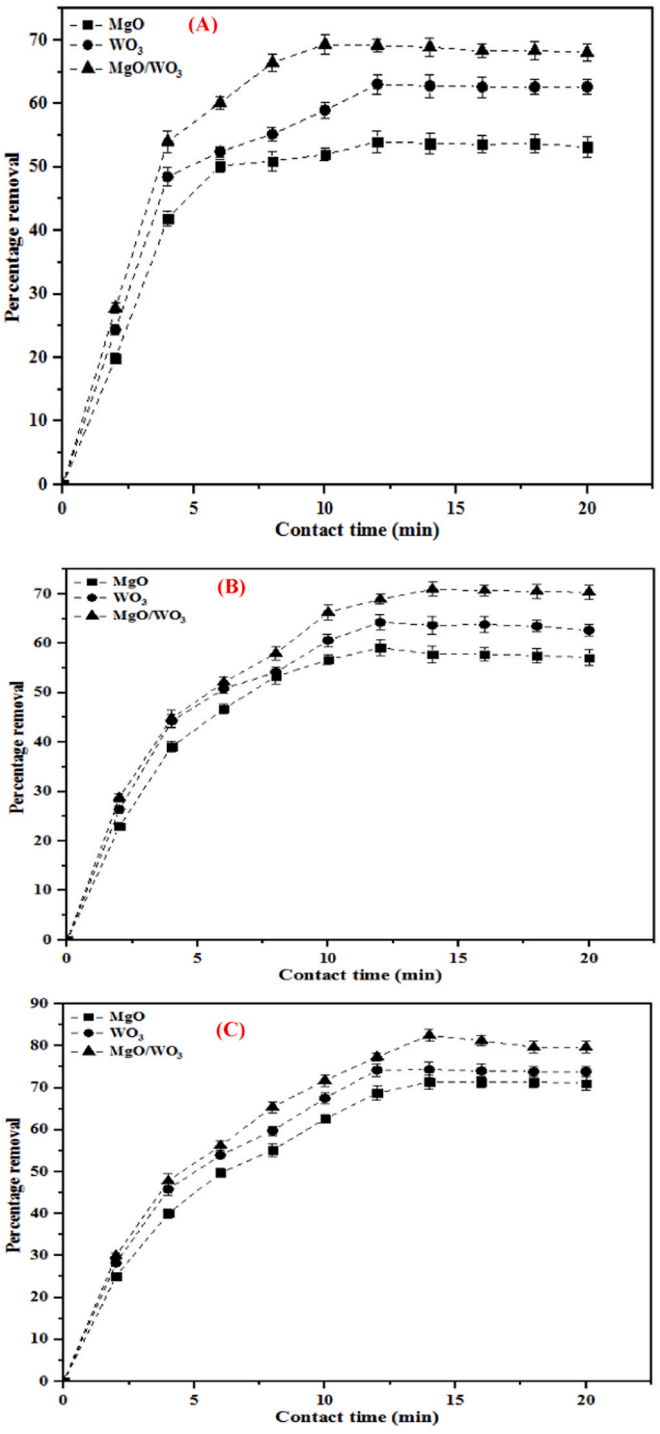

Fig. 7. Effect of contact time on the removal of (A) Cu(II); (B) Fe(II) and (C) Cr(VI) ions at dosage (0.2 g), temperature (25 °C), pH (9.98) and agitation speed (150 rpm).

times were reached. The maximum percentage removal of Cu(II), Fe (II) and CrVI) ions onto MgO nanoadsorbent was 54.3%, 59.5% and 72.0% at the optimum time of 12, 12 and 14 min, respectively. For WO_3 nanoadsorbent, the maximum removal efficiency of Cu(II), Fe (II) and Cr(VI) ions were 63.0%, 64.2% and 74.6% at an equilibrium time of 12 min each.

Correspondingly, the nanocomposites (MgO/WO_3) exhibited maximum adsorption removal of Cu(II) ion (69.4%), Fe(II) ion (71.0%)

and Cr(VI) ion (82.9%) at optimum time of 10 min. The rapid adsorption of the metals ions before equilibrium time could be attributed to the availability of large vacant active sites on the surface of nanoadsorbents. Thus, beyond the optimum contact time, the number of vacant active sites on the nanoadsorbent reduced, leading to the desorption stage. A similar trend was noticed by Chowdhury et al. (2016) and Madzokere and Karthigeyan (2017) who independently worked on the removal of Pb(II) and Cu(II) ions on mesoporous MgO nanostructure and adsorption of Cu(II) by nano-MgO, respectively. They observed that the initial rapid adsorption rate was because of abundant sites on the surface of the MgO nanoadsorbent. It was also observed that Cr(VI) ion was mostly removed from the dyeing wastewater by the nanoadsorbents under the same conditions than other metal ions. The order of removal of heavy metals from local dyeing wastewater follows the order; Cr > Fe > Cu. This behaviour could be linked to differences in ionic radii of the metal ions in the dyeing wastewater. It was noticed that metal ions with smaller ionic radii diffused faster than others. Comparatively, it was observed that MgO/WO_3 nanoadsorbent exhibited excellent removal efficacy of the target pollutants from the wastewater than the individual MgO and WO_3 nanoadsorbent. This could be attributed to the existence of synergetic effects responsible for the higher specific surface area exhibited by MgO/WO_3 nanocomposites than WO_3 alone.

3.7.2. Effect of adsorbent dosage

The adsorbent dosage is a significant parameter in the adsorption experiment and the effect of adsorbent dosage ranging from 0.2 to 1.0 g on the percentage removal of Cu(II), Fe(II) and Cr(VI) ions was investigated and the result is presented in Fig. 8 (A-C). As can be seen in the adsorption of pollutants, the removal percentage increased with an increasing amount of nanoadsorbent dosage. The removal efficiencies of Cu(II) ion increased from 38.1% to 92.1%, 43.2–98.1% and 45.7–100% for MgO, WO_3 and MgO/WO_3 nanoadsorbents. A similar increment in the removal of Fe(II) ion from the wastewater from 40.45% to 94.0%, 44.6–99.5% and 49.8–100% was observed. The removal of Cr(VI) ion from the dye wastewater also increased from 42.5% to 95.1%, 47.4–99.0% and 51.0–100% using MgO, WO_3 and MgO/WO_3 as nanoadsorbents.

The increase in adsorption efficiency with the dose could be attributed to the availability of more binding sites and enhanced surface area of the material. Cr(VI) (0.052 nm) with the smallest ionic radius and highest electronegativity removed more than Cu(II) (0.073 nm) and Fe(II) (0.0645 nm) with higher ionic radii. Thus, the adsorption efficiency of the heavy metals followed this order: Cr > Fe > Cu. This implies that the smaller the ionic radii, the faster the rate of diffusion and removal efficiency. This is in agreement with the reports of Egbosiuba et al. (2020) and Mustapha et al. (2021). This study did not follow the report of Kaveeshwar et al. (2018). The author emphasized that the differences in adsorption were based on ionic radii, suggesting that metal ions with large ionic radii can induce fast onto the adsorption site due to steric and overcrowding on the surface of the adsorbent than metal with a smaller ionic radius. In contrast, there was no significant increase in the removal efficiency of the target metal ions between the adsorbent dosage of 0.8 and 1.0 g. This behaviour was ascribed to oversaturation of the adsorbent active sites or the existence of strong competition between the target pollutants and other scavengers in the aqueous solution for the active sites.

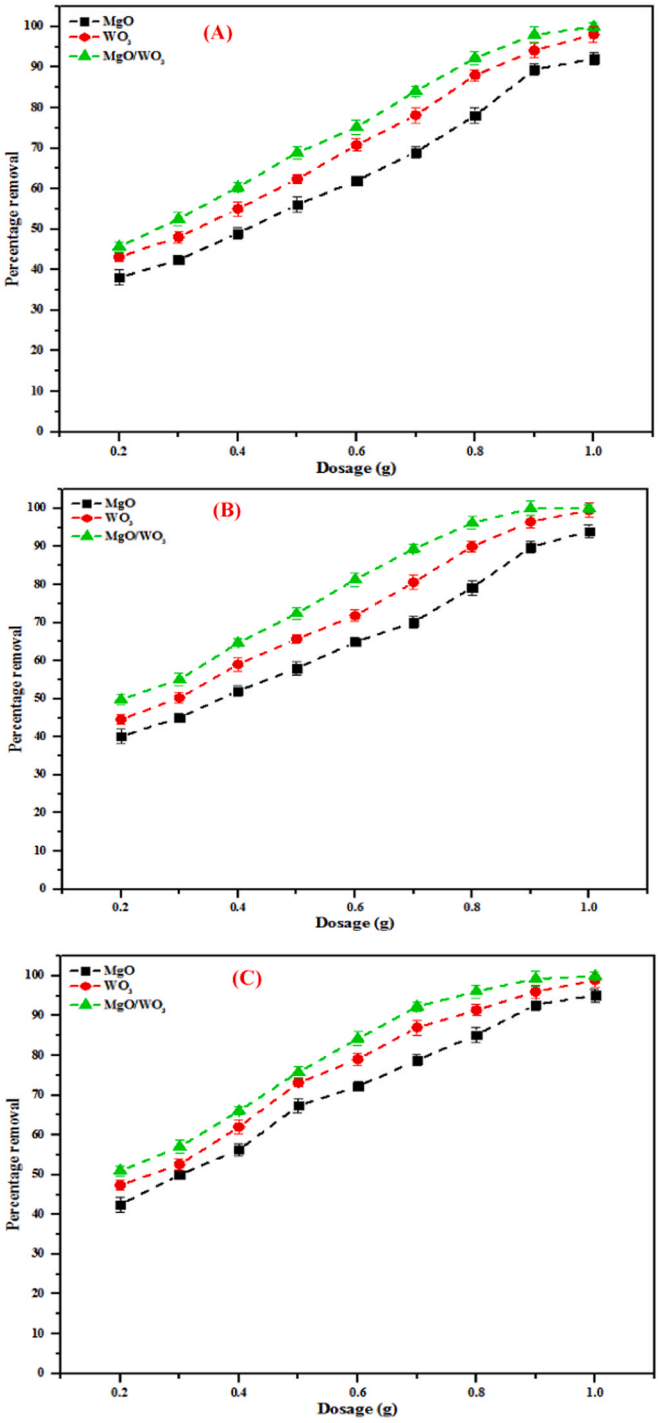

Fig. 8. Effect of dosage on the removal of (A) Cu(II); (B) Fe(II) and (C) Cr(VI) ions at the optimum time (10 min), temperature (25 °C), pH (9.98) and agitation speed (150 rpm).

3.7.3. Effect of temperature

Temperature affects the adsorptive capacity of nanoadsorbent and also enhances the diffusion rate of adsorbate across the external boundary and internal pores of adsorbent particles (Miyah et al.,

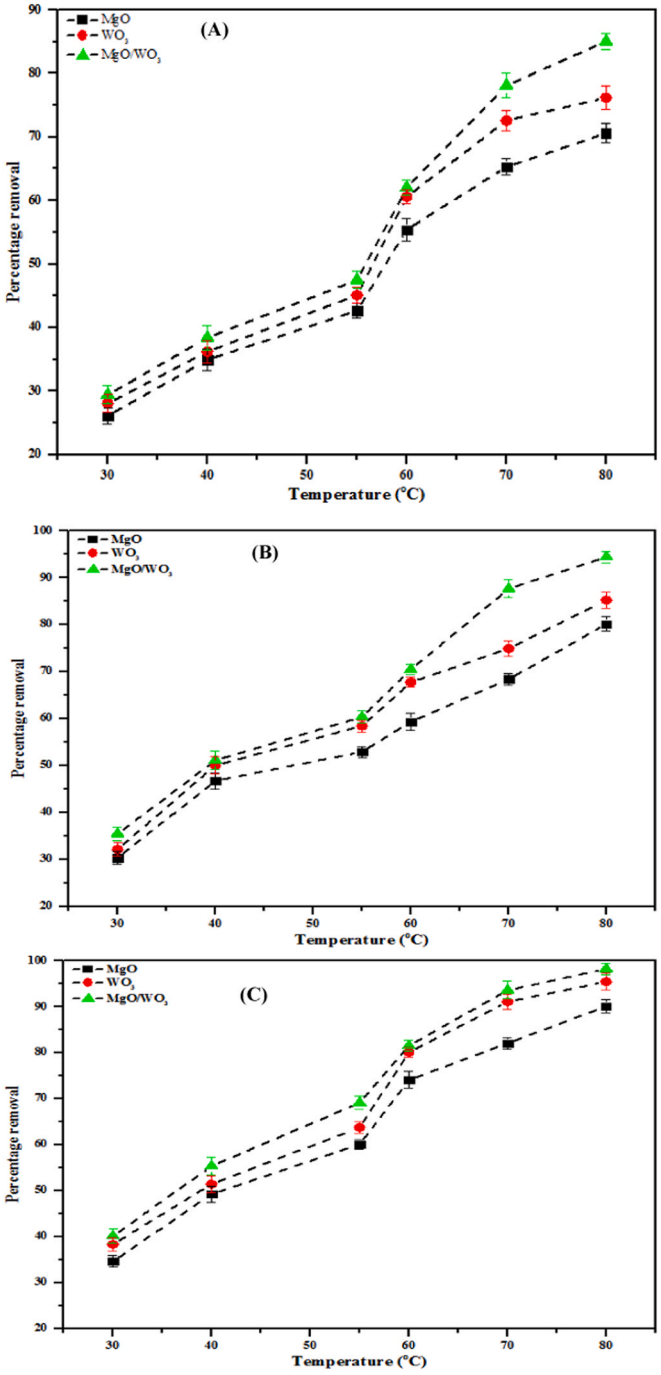

Fig. 9. Effect of temperature on the removal of (A) Cu(II); (B) Fe(II) and (C) Cr(VI) ions at the optimum time (10 min), dosage (0.2 g), pH (9.98) and agitation speed (150 rpm).

2018). The effect of temperature on the removal of Cu(II), Fe(II) and Cr(VI) ions at a temperature ranging from 30 to 80 °C was investigated and the result is presented in Fig. 9 (A-C).

It was observed that the adsorption efficiency of the selected heavy metals increased with temperature due to the increased mobility of the adsorbate onto the active sites of the nanoadsorbents. This suggests that an increase in temperature is favoured and benefits the removal of the heavy metals, which is evidence of the endothermic behaviour of the adsorbed pollutants on MgO, WO_3 and MgO-WO_3 nanoadsorbents. This effect could initiate a chemical reaction or bond formation between the adsorbent and the adsorbate. A similar observation was reported by Kumar et al. (2018). In addition, high temperature increases the movement of metal ions from the bulk of the liquid to the surface of the nanoadsorbent, thus leading to the formation of new effective sites. The complete removal of Cu(II), Fe(II) and Cr(VI) ions were not achieved which could be attributed to the strong competition for the adsorption sites by other interfering ions with the target metals or the blocking of adsorbent sites by TDS or TSS in the aqueous media.

3.8. Adsorption isotherm models

The experimental data were obtained from the adsorption of Cu (II), Fe(II) and Cr(VI) ions at a temperature ranging from 30 to 80 °C by MgO, WO_3 and MgO-WO_3 nanoadsorbents were subjected to different adsorption isotherms. The experimental data were fitted using linearized regression co-efficient according to the Freundlich, Langmuir and Temkin isotherm models and the results are presented in Table 2. The fitness of the experimental data was determined with the regression correlation coefficient (R^2). It was found that the Langmuir model most suited model compared to Freundlich and Temkin isotherms. This suggests complete monolayer coverage of the homogeneous surface.

The pollutants were adsorbed onto the homogeneous binding sites and the results agreed with the finding of Xu et al. (2020). The value of adsorption intensity (n) values obtained from the Freundlich model lies between 2 and 10, indicating the nanoadsorbents are good for the removal of pollutants. With regards to the correlation coefficient, this isotherm model did not fit well with the experimental data. In addition, it is also stated that the use of these isotherms could tacitly change the error variance and normality assumption of standard least squares (Almasian et al., 2017). For authenticity of the fitness of isotherm models and the fitness of the equation to the experimental data, error functions were evaluated. In this work, Chi-square (χ^2) and the sum of square error (SSE) tests were used to buttress the best-fit isotherm model (see Table 2). The lower the error function, the better the isotherm model used for the adsorption of pollutants onto the nanoadsorbents. As can be seen from Table 2, the Langmuir isotherm has the least error function values, showing that the adsorption of the pollutant from dyeing wastewater strictly follows the Langmuir model. An overall observation of the three-isotherm models employed in terms of correlation coefficient and error function analysis revealed that the isotherm follows this trend: Langmuir > Temkin > Freundlich.

The maximum adsorption capacities of Cu(II), Fe(II) and Cr(VI) ions using MgO-WO_3 nanoadsorbents as presented in Table 3 were compared with the adsorption capacities of previously prepared adsorbents. It was found that as-prepared MgO-WO_3 had the highest adsorption capacity in comparison to the earlier reported

Table 2
Adsorption isotherm parameters of Cu(II), Fe(II) and Cr(VI) ions form local dyeing wastewater.

Isotherm	Parameter	Cu (II)			Fe (II)			Cr (VI)		
		WO_3	MgO	MgO/WO_3	WO_3	MgO	MgO/WO_3	WO_3	MgO	MgO/WO_3
Langmuir	Q_m	120.31	125.39	128.82	128.65	132.03	135.76	157.73	162.04	165.95
	K_L	4.05×10^{-3}	3.98×10^{-3}	3.92×10^{-3}	3.99×10^{-3}	3.96×10^{-3}	4.12×10^{-3}	1.46×10^{-2}	1.54×10^{-2}	1.59×10^{-2}
	R^2	0.99183	0.99483	0.99662	0.98838	0.98868	0.99453	0.99269	0.99356	0.99799
	SSE	21.09	17.30	13.60	32.17	28.80	19.03	14.09	9.65	5.072
	χ^2	10.54	6.74	4.32	8.11	5.62	2.31	6.04	4.01	2.06
Freundlich	K_F	0.083	0.091	0.099	0.096	0.103	0.117	0.0785	0.086	0.089
	n	1.48×10^{-4}	3.31×10^{-4}	7.19×10^{-4}	6.39×10^{-4}	1.051×10^{-3}	2.718×10^{-3}	1.370×10^{-3}	2.96×10^{-3}	7.20×10^{-3}
	R^2	0.98808	0.98954	0.99043	0.96096	0.98698	0.98925	0.98650	0.99111	0.99352
	SSE	25.70	19.99	17.05	38.56	34.38	27.22	21.08	16.59	15.03
	χ^2	16.64	15.01	12.88	12.90	10.53	8.39	8.97	7.50	5.16
Temkin	B_T	5.450	5.035	4.636	4.831	4.562	4.038	4.238	3.895	3.772
	A_T	0.126	0.127	0.129	0.132	0.133	0.135	0.0544	0.0564	0.0566
	R^2	0.98666	0.99099	0.99185	0.98106	0.98587	0.98882	0.98923	0.99139	0.99196
	SSE	23.05	16.60	14.22	34.52	31.08	23.45	16.63	10.81	8.03
	χ^2	12.09	8.11	7.70	9.08	6.44	3.54	5.27	5.02	3.75

Table 3
Comparison of adsorption capacity of MgO-WO_3 adsorbent for metal ion removal with previous literature.

Adsorbent	Adsorption capacity (mg/g)	Metal ion	Experimental condition	References
Fe_3O_4/Activated carbon	3.2	Cu(II)	Contact time 3 h, shaking speed 180 rpm, pH 2, Temperature 25 °C	Jain et al. (2018)
$MnFe_2O_4$	91.24	Cr(VI)	Dosage 1.0 g/L, pH 2	Bhownik et al. (2017)
EDTA/Bentonite	27	Cu(II)	Contact time 120 min, Temperature 30 °C	De-castro et al. (2018)
Fe°/Rubber seed shell	48.18	Cu(II)	Contact time 30 min, pH 6, Dosage 3 g/L, Temperature 30 °C	Prabu et al. (2017)
Nanoperlite	16.67	Fe(II)	Dosage 0.15 g, pH 3.2, Concentration 50 mg/L	Shabani et al. (2017)
CuS/*Phyllostachys pubescens*	52.30	Cr(VI)	Contact time 2 h, Dosage 2 g/L, pH 6.1, Temperature 25 °C	Ai et al. (2018)
Waste glass	10.31	Fe(II)	Contact time 45 min, Dosage 1.5 g/L, Temperature 25 °C	Rashed et al. (2018)
Activated carbon	7.76	Fe(II)	Contact time 60 min, Dosage 0.1 g, Temperature 25.15 °C, Pressure 101 kPa	Maneechakr and Karnjanakom (2017)
Nickel ferrite/Graphene oxide	20.58	Cr(VI)	Contact time 30 min, pH 4, Temperature 25–55 °C	Lingamdinne et al. (2017)
MgO/WO_3	128.82	Fe(II)	Contact time 15 min, pH 9.98, Dosage 0.1 g, Temperature 30–80 °C	This study
MgO/WO_3	135.76	Cu(II)	Contact time 10 min, pH 9.98, Dosage 0.1 g, Temperature 30–80 °C	This study
MgO/WO_3	165.95	Cr(VI)	Contact time 15 min, pH 9.98, Dosage 0.1 g, Temperature 30–80 °C	This study

Table 4
Adsorption kinetic parameters of Cu(II), Fe(II) and Cr(VI) ions from local dyeing wastewater.

Pollutant	Adsorbent	First-order					Second-order					Intra-particle diffusion				
		k_1	q_e	R^2	SSE	χ^2	k_2	q_e	R^2	SSE	χ^2	K_i	I	R^2	SSE	χ^2
Cu(II)	WO_3	0.103	0.245	0.5233	102.12	14.01	0.712	1.334	0.9810	91.81	8.20	0.0102	0.162	0.7810	95.05	11.19
	MgO	0.162	0.387	0.5818	88.09	10.02	0.851	1.561	0.9940	75.20	7.65	0.0151	0.240	0.7922	82.31	8.35
	MgO/WO_3	0.180	0.407	0.6551	81.09	7.90	0.910	1.938	0.9980	72.52	5.44	0.0184	0.284	0.8051	75.74	6.53
Fe(II)	WO_3	0.275	0.598	0.5520	98.81	12.60	0.612	1.302	0.9620	73.46	8.09	0.0098	0.158	0.6410	79.03	10.28
	MgO	0.306	0.740	0.6466	80.63	9.31	0.701	1.510	0.9770	69.50	7.29	0.0110	0.213	0.6876	78.01	8.92
	MgO/WO_3	0.494	0.862	0.6951	74.23	7.24	0.821	1.640	0.9800	62.72	4.12	0.0163	0.275	0.7081	70.71	5.15
Cr(VI)	WO_3	0.580	1.227	0.6607	74.18	5.96	0.925	2.329	0.9903	63.26	4.33	0.0175	0.189	0.7984	68.41	5.81
	MgO	0.774	1.387	0.6718	72.32	4.99	1.012	2.420	0.9920	60.12	4.03	0.0240	0.261	0.8449	66.35	4.53
	MgO/WO_3	0.864	1.965	0.6979	67.45	3.97	1.260	2.617	0.9990	58.47	2.10	0.0287	0.290	0.9039	63.86	3.80

adsorbents. This can be attributed to the higher specific surface area of the as-synthesized MgO-WO_3 nanocomposites and the meso-porosity nature of the material. This implies that binary metal oxides removed more pollutants from wastewater than individual metal oxides.

3.9. Adsorption kinetic models

Adsorption studies were conducted for the removal of Cu(II), Fe (II) and Cr(VI) ions from dyeing wastewater using MgO, WO_3 and MgO/WO_3 nanoadsorbents. The adsorption data on the removal of

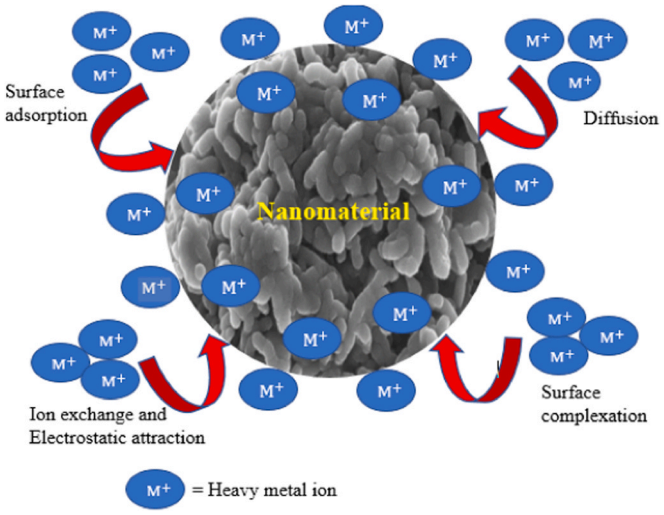

Fig. 10. Proposed adsorption mechanism.

pollutants from dyeing wastewater were subjected to kinetic analysis and the result is presented in Table 4. From Table 4, the kinetic model parameters for adsorption of pollutants were fitted into pseudo-first-order, pseudo-second-order models and intra-particle diffusion. Based on the value of the correlation coefficient (R^2), the adsorption of the target metals ions shows better agreement with the pseudo-second-order model. This suggests that the adsorption of metal ions is directly proportional to the number of active sites and surface area of the nanoadsorbents. This means that chemisorption played a significant role in the adsorption process (Xu et al., 2020). Additionally, the chemisorption process could be linked to the exchange of electrons between functional groups on the adsorbent and target metal ions in the medium during valance force. Noticeably, the calculated k_2 value was highest for Cr(VI) ion followed by Fe(II) and Cu(II) ions, which was based on the ionic radius mechanism of the adsorbed metal ions on the nanoadsorbents. This is confirmed by the report of Mustapha et al. (2021) who stated that the less the hydrated ionic radius the higher is the rate constant value of the pseudo-second-order. The surface of nanoadsorbent captured metal ions by diffusion, ion exchange process surface adsorption, electrostatic interaction and surface complexation. This implies that the surface of the MgO-WO_3 nanocomposite has a strong affinity for the adsorption of metal ions from dyeing wastewater than WO_3 and MgO respectively. Also, the adsorption process was found to be dependent on dosage and surface functionality leading to selective adsorption of the metal ions onto the nanomaterials.(Fig. 10)

3.10. Thermodynamic study

The thermodynamic studies of Cu(II), Fe(II) and Cr(VI) ions removal by the nanoadsorbents were examined at the temperature range of 30–80 °C. This was done to establish the spontaneity and non-spontaneity of the adsorption of the heavy metals by the nanoadsorbents. The thermodynamic parameters such as a change in enthalpy, change in entropy and change in free Gibb's energy were determined and the values are presented in Table 5. The values of ΔH were all positive irrespective of the nanoadsorbents and the positive values of Δ*H* revealed that the adsorption process was endothermic. The positive values of ΔS also confirmed an increase in the degree of disorderliness and randomness of the adsorbate-nanoadsorbent interface during the adsorption of the metal ions. The negative values of ΔG for the adsorption of pollutants onto nanoadsorbents indicate that the adsorption of Cu(II), Fe(II) and Cr(VI) ions was thermodynamically spontaneous and feasible. Xu et al. (2020) reported similar observations on the adsorption of Pb(II) and Cu(II) ions onto SiO_2/MgO nanofibers. They found that ΔG at all temperatures for the adsorption of metal ions were negative and spontaneous. Therefore, it can be inferred that at a higher temperature, the adsorption process increased due to higher adsorption capacity.

3.11. Regeneration study

The regeneration studies were evaluated to determine the reusability/stability of the nanoadsorbents (MgO, WO_3 and MgO-WO_3). The percentage removal of the nanoadsorbents after each cycle is presented in Fig. 11 (A-C). The results showed that the MgO-WO_3 nanocomposites have the highest removal efficiency for Cu(II), Fe(II) and Cr(VI) ions even after 5 repeated cycles.

The percentage removal for MgO and WO_3 nanoparticles was still high at cycle 3, but subsequently dropped as the number of cycles increased. This implies that the two materials cannot be used repeatedly beyond 3 cycles. This suggests the total collapse of the inner and outer pores or gradual blockage of the active sites by the metal ions. The adsorption capacity of the MgO-WO_3 nanocomposites did not indicate any significant decrease in adsorption of Cr(VI), Fe(II) and Cu(II) ions even after 5 cycles. This behaviour could be linked to the surface area and adsorption capacities of MgO-WO_3. The stability of the nanocomposites demonstrated that the

Table 5
Thermodynamic parameters of Cu(II), Fe(II) and Cr(VI) ions onto MgO, WO_3 and MgO/WO_3 nanoadsorbents from local dyeing wastewater.

Pollutant	Adsorbent	ΔG(kJ/mol)								
		ΔH(kJ/mol	ΔS(J/mol/K	R^2	303 K	313 K	323 K	333 K	343 K	353 K
Cu(II)	MgO	20.00	73.32	0.9187	-2.22	-2.95	-3.68	-4.42	-5.15	-5.88
	WO_3	34.89	114.34	0.9678	0.25	-0.90	-2.04	-3.19	-4.33	-5.47
	MgO/WO_3	21.22	76.48	0.9740	-1.95	-2.72	-3.48	-4.25	-5.01	-5.78
Fe(II)	MgO	24.77	82.13	0.8574	-0.11	-0.94	-1.76	-2.58	-3.40	-4.22
	WO_3	17.11	62.92	0.8700	-1.96	-2.58	-3.21	-3.84	-4.47	-5.10
	MgO/WO_3	18.73	67.16	0.9330	-1.62	-2.29	-2.96	-3.63	-4.31	-4.98
Cr(VI)	MgO	24.51	81.71	0.9441	-0.25	-1.07	-0.188	-2.70	-3.52	-4.33
	WO_3	17.48	65.76	0.8926	-2.45	-3.10	-3.76	-4.42	-5.08	-5.73
	MgO/WO_3	16.80	63.28	0.8877	-2.38	-3.01	-3.64	-4.27	-4.91	-5.54

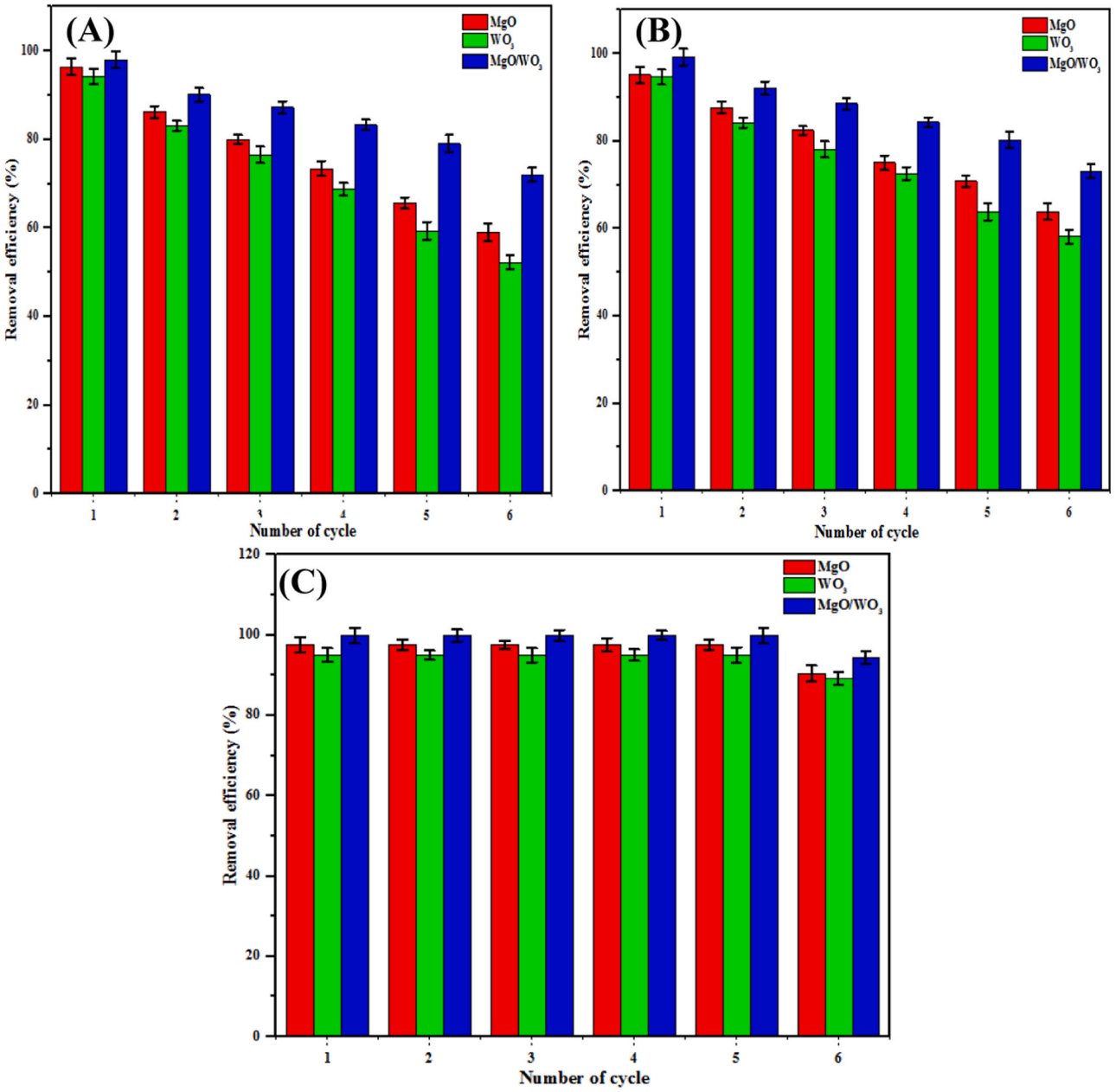

Fig. 11. Reusability cycles using MgO, WO_3 and MgO-WO_3 for (A) Fe(II), (B) Cu(II) and (C) Cr(VI) removal.

nanoadsorbent possessed high adsorption properties for the removal of metal ions. The regenerated adsorbents may be employed for industrial applications.

4. Conclusion

The synthesis, characterization and application of bio/wet impregnation synthesised MgO-WO_3 nanocomposites for the treatment of Indigenous dyeing wastewater were examined. The as-prepared MgO, WO_3 and MgO-WO_3 nanoadsorbents were specifically used for the sequestration of Cu(II), Fe(II) and Cr(VI) ions in dyeing wastewater. Batch adsorption experiments were conducted under the influence of contact time, nanoadsorbent dosage and temperature. The isotherm, kinetic and regeneration studies were described in this study. The following conclusions were drawn based on the results obtained.

- The nanoadsorbents were synthesized using a green method, which showed the monoclinic crystalline phase of WO_3, face centred cubic periclase phase of MgO nanoparticles, and the existence of chemical reactions between MgO and WO_3 nanocomposites leading to the formation of a new material $MgWO_4$.
- The HRSEM, HRTEM, BET, EDX and SAED revealed the presence of MgO and WO_3 nanoparticles in their composites at different mixing ratios. XRD confirmed the formation of magnesium tungstate ($MgWO_4$) nanoparticles irrespective of the mixing ratios.
- The adsorption process was contact time, adsorbent dosage and temperature-dependent. The maximum removal efficiency of Cu (II), Fe(II) and Cr(VI) at an optimum contact time of 12, 12 and 14 min and adsorbent dosage of 1.0 g is 98.1%, 100% and 100%, respectively.
- The adsorption data were better described by the Langmuir isotherm model and pseudo-second-order kinetic model. The

thermodynamic study demonstrated that the adsorption of the selected heavy metals was endothermic, feasible and spontaneous in nature

- A regeneration study showed that the adsorption of Cr(VI), Fe(II) and Cu(II) ions using MgO-WO_3 nanocomposite from local dyeing wastewater after six consecutive cycles did not change from the initial amount removed. This suggested the suitability of MgO-WO_3 nanocomposite for repeated application in wastewater treatment technology.

Declaration of competing interest

The authors declared that they have no conflict of interest.

Acknowledgements

The authors appreciate the contribution of the following people for their technical assistance: Dr Remy Bucher (XRD analysis, iThemba Labs, South Africa) and Dr Franscious Cummings (HRSEM/HRTEM/SAED/EDS) analysis, Physics department, University of the Western Cape (UWC), South Africa.

Availability of data and materials

The data generated or analyzed during this study are included in this published article. The datasets used are available from the corresponding author on reasonable request.

Author contribution

Chris Agida Uko-conceptualization, analysis and major contributor in writing the manuscript. Jimoh Oladejo Tijani, Ambali Saka Abdulkareem, Saheed Mustapha and Edison Muzenda interpreted the results, proofread, edited and approved the final version of the manuscript.

Funding

The authors acknowledged Tertiary Education Trust Fund, Nigeria, with grant number (TETFUND/FUTMINNA/2016–2017/6th BRP/11) for the sponsorship.

Ethics approval and consent to participate

Not applicable.

Consent for publication

Not applicable.

Appendix A. Supporting information

Supplementary data associated with this article can be found in the online version at doi:10.1016/j.psep.2022.04.057.

References

Abinaya, S., Kavitha, H.P., Prakash, M., Muthukrishnaraj, A., 2021. Green synthesis of magnesium oxide nanoparticles and its applications: a review. Sustain. Chem. Pharm. 19, 100368.

Abshirini, Y., Esmaeili, H., Foroutan, R., 2019. Enhancement removal of Cr (VI) ion using magnetically modified MgO nanoparticles. Mater. Res. Express 6 (12), 125513.

Ahmed, M.A., Abou-Gamra, Z.M., 2016. Mesoporous MgO nanoparticles as a potential sorbent for removal of fast orange and bromophenol blue dyes. Nanotechnol. Environ. Eng. 1, 10.

Ai, T., Jiang, X., Liu, Q., 2018. Chromium removal from industrial wastewater using Phyllostachys pubescens biomass loaded Cu-S nanospheres. Open Chem. 16 (1), 842–852.

Alalwan, H.A., Kadhom, M.A., Alminshid, A.H., 2020. Removal of heavy metals from wastewater using agricultural byproducts. J. Water Supply.: Res. Technol. -Aqua 69 (2), 99–112.

American Public Health Association (APHA), 2017. Standard Methods for the Examination of Water and Wastewater, twentyfirst ed. APHA American Public Health Association, Washington, D.C.

Asha, S., Asha, A., Rajeshkumar, S., 2017. Evaluation of phytochemical constituents and antimicrobial activity of silver nanoparticle synthesized Ipomoea nil against selected pathogens. Asian J. Pharm. Clin. Res. 10, 183–187.

Bear, S.E., Nguyen, M.T., Jasper, J.T., Nygren, S., Nelson, K.L., Sedlak, D.L., 2017. Removal of nutrients, trace organic contaminants, and bacterial indicator organisms in a demonstration-scale unit process open-water treatment wetland. Ecol. Eng. 109, 76–83.

Bhowmik, K.L., Debnath, A., Nath, R.K., Saha, B., 2017. Synthesis of $MnFe_2O_4$ and Mn3O4 magnetic nano-composites with enhanced properties for adsorption of Cr (VI): artificial neural network modeling. Water Sci. Technol. 76 (12), 3368–3378.

Cai, Y., Li, C., Wu, D., Wang, W., Tan, F., Wang, X., Wong, P.K., Qiao, X., 2017. Highly active MgO nanoparticles for simultaneous bacterial inactivation and heavy metal removal from aqueous solution. Chem. Eng. J. 312, 158–166.

Chockalingam, N., Banerjee, S., Muruhan, S., 2019. Characterization of physicochemical parameters of textile effluents and its impacts on environment. Environ. Nat. Resour. J. 17 (2), 41–53.

Chowdhury, I.H., Chowdhury, A.H., Bose, P., Mandal, S., Naskar, M.K., 2016. Effect of anion type on the synthesis of mesoporous nanostructured MgO, and its excellent adsorption capacity for the removal of toxic heavy metal ions from water. RSC Adv. 6 (8), 6038–6047.

De Castro, M.L.F.A., Abad, M.L.B., Sumalinog, D.A.G., Abarca, R.R.M., Paoprasert, P., de Luna, M.D.G., 2018. Adsorption of methylene blue dye and Cu(II) ions on EDTA-modified bentonite: isotherm, kinetic and thermodynamic studies. Sustain. Environ. Res. 28 (5), 197–205.

Durotoye, T.O., Adeyemi, A.A., Omole, D.O., Onakunle, O., 2018. Impact assessment of wastewater discharge from a textile industry in Lagos, Nigeria. Cogent Eng. 5 (1), 1531687.

Egbosiuba, T.C., Abdulkareem, A.S., Kovo, A.S., Afolabi, E.A., Tijani, J.O., Auta, M., Roos, W.D., 2020. Ultrasonic enhanced adsorption of methylene blue onto the optimized surface area of activated carbon: adsorption isotherm, kinetics and thermodynamics. Chem. Eng. Res. Des. 153, 315–336.

Elgarahy, A.M., Elwakeel, K.Z., Mohammad, S.H., Elshoubaky, G.A., 2021. A critical review of biosorption of dyes, heavy metals and metalloids from wastewater as an efficient and green process. Clean. Eng. Technol. 4, 100209.

Hafez, M., Popov, A.I., Rashad, M., 2020. A novel environmental additive to decrease nitrate level in agriculture wastewater and enhancement nutrient status under greenhouse plant growth in calcareous soil. Plant Arch. 20, 3165–3172.

Ismail, M., Akhtar, K., Khan, M.I., Kamal, T., Khan, M.A., M Asiri, A., Seo, J., Khan, S.B., 2019. Pollution, toxicity and carcinogenicity of organic dyes and their catalytic bio-remediation. Curr. Pharm. Des. 25 (34), 3645–3663.

Jain, M., Yadav, M., Kohout, T., Lahtinen, M., Garg, V.K., Sillanpää, M., 2018. Development of iron oxide/activated carbon nanoparticle composite for the removal of Cr(VI), Cu(II) and Cd(II) ions from aqueous solution. Water Resour. Ind. 20, 54–74.

Jamali, M, Tehrani, F. S, 2020. Effect of synthesis route on the structural and morphological properties of WO_3 nanostructures. Mat. Sci. Semicon. Proc. 107, 104829.

Jamil, N., Mehmood, M., Lateef, A., Nazir, R., Ahsan, N., 2015. MgO Nanoparticles for the Removal of Reactive dyes from Wastewater. Advanced Materials: TechConnect Briefs.

Kadhom, M., Albayati, N., Alalwan, H., Al-Furaiji, M., 2020. Removal of dyes by agricultural waste. Sustain. Chem. Pharm. 16, 100259.

Karimi-Maleh, H., Orooji, Y., Ayati, A., Qanbari, S., Tanhaei, B., Karimi, F., Alizadeh, M., Rouhi, J., Fu, L., Sillanpää, M., 2020. Recent advances in removal techniques of Cr (VI) toxic ion from aqueous solution: A comprehensive review. J. Mol. Liq. 392, 115062.

Karthik, K., Dhanuskodi, S., Gobinath, C., Prabukumar, S., Sivaramakrishnan, S., 2019. Ultrasonic-assisted CdO–MgO nanocomposite for multifunctional applications. Mater. Technol. 34 (7), 403–414.

Kaveeshwar, A. R, Kumar, P. S, Revellame, E. D, Gang, D. D, Zappi, M. E, Subramaniam, R, 2018. Adsorption properties and mechanism of barium (II) and strontium (II) removal from fracking wastewater using pecan shell based activated carbon. J. Clean. Prod. 193, 1–13.

Kumar, T.V., Sivasankar, V., Fayoud, N., Abou Oualid, H., Sundramoorthy, A.K., 2018. Synthesis and characterization of coral-like hierarchical MgO incorporated fly ash composite for the effective adsorption of azo dye from aqueous solution. Appl. Surf. Sci. 449, 719–728.

Lai, C.W., 2015. WO_3 nanoplates film: formation and photocatalytic oxidation studies. J. Nanomater. 2015, 1–8.

Lei, R., Zhang, H., Ni, H., Chen, R., Gu, H., Zhang, B., 2018. Novel ZnO nanoparticles modified WO_3 nanosheet arrays for enhanced photocatalytic properties under solar light illumination. Appl. Surf. Sci. 463, 363–373.

Lingamdinne, L.P., Kim, I.S., Ha, J.H., Chang, Y.Y., Koduru, J.R., Yang, J.K., 2017. Enhanced adsorption removal of Pb(II) and Cr(III) by using nickel ferrite-reduced graphene oxide nanocomposite. Metals 7 (6), 225.

Lu, R., Zhong, X., Shang, S., Wang, S., Tang, M., 2018. Effects of sintering temperature on sensing properties of WO_3 and Ag-WO_3 electrode for NO_2 sensor. R. Soc. Open Sci. 5 (10), 171691 Chicago.
Madzokere, T.C., Karthigeyan, A., 2017. Heavy Metal Ion Effluent Discharge Containment Using Magnesium Oxide (MgO) Nanoparticles. Mater. Today.: Proc. 4 (1), 9–18.
Maharana, M., Manna, M., Sardar, M., Sen, S., 2021. Heavy Metal Removal by Low-Cost Adsorbents. Green Adsorbents to Remove Metals, Dyes and Boron from Polluted Water. Springer,, Cham, pp. 245–272.
Mahdavi, S., Hassani, A., Merrikhpour, H., 2020. Aqueous phosphorous adsorption onto SnO_2 and WO_3 nanoparticles in batch mode: kinetic, isotherm and thermodynamic study. J. Exp. Nanosci. 15 (1), 242–265.
Maneechakr, P., Karnjanakom, S., 2017. Adsorption behaviour of Fe(II) and Cr(VI) on activated carbon: Surface chemistry, isotherm, kinetic and thermodynamic studies. The. J. Chem. Thermodyn. 106, 104–112.
Manjunatha, A.S., Pavithra, N.S., Shivanna, M., Nagaraju, G., Ravikumar, C.R., 2020. Synthesis of Citrus limon mediated SnO_2-WO_3 nanocomposite: Applications to photocatalytic activity and electrochemical sensor. J. Environ. Chem. Eng. 8 (6), 104500.
Mishra, S., Bharagava, R.N., More, N., Yadav, A., Zainith, S., Mani, S., Chowdhary, P., 2019. Heavy metal contamination: an alarming threat to environment and human health. Environmental Biotechnology: For Sustainable Future. Springer, Singapore, pp. 103–125.
Miyah, Y., Lahrichi, A., Idrissi, M., Khalil, A., Zerrouq, F., 2018. Adsorption of methylene blue dye from aqueous solutions onto walnut shells powder: equilibrium and kinetic studies. Surf. Interfaces 11, 74–81.
Moustafa, I.M.I., Saleh, I.A., Abdelhami, M.R., 2017. Synthesis of MgO nanoparticles from different organic precursors: catalytic decontamination of organic pollutants and antitumor activity. J. Mater. Sci. Eng. 6 (4), 1–8.
Mustapha, S., Tijani, J.O., Ndamitso, M.M., Abdulkareem, A.S., Shuaib, D.T., Mohammed, A.K., 2021. Adsorptive removal of pollutants from industrial wastewater using mesoporous kaolin and kaolin/TiO_2 nanoadsorbents. Environ. Nanotechnol., Monit. Manag. 15, 100414.
Naik, K., Mishra, S., Srichandan, H., Singh, P.K., Sarangi, P.K., 2019. Plant growth promoting microbes: Potential link to sustainable agriculture and environment. Biocatal. Agric. Biotechnol. 21, 101326.
Nigerian Industrial Standard (NIS), 2007. Nigerian Standard for Drinking Water Quality. NIS554. Stand. Organ. Niger. 2007, 1–30.
Obasi, P.N., Akudinobi, B.B., 2020. Potential health risk and levels of heavy metals in water resources of lead–zinc mining communities of Abakaliki, southeast Nigeria. Appl. Water Sci. 10 (7), 1–23.
Pensupa, N., Leu, S.Y., Hu, Y., Du, C., Liu, H., Jing, H., Wang, H., Lin, C.S.K., 2017. Recent trends in sustainable textile waste recycling methods: current situation and future prospects. Chem. Chem. Technol. Waste Valoriz. 189–228.
Prabu, D., Parthiban, R., Ponnusamy, S.K., Anbalagan, S., John, R., Titus, T., 2017. Sorption of Cu (II) ions by nano-scale zero valent iron supported on rubber seed shell. IET Nanobiotechnol. 11 (6), 714–724.
Rashed, M.N., Gad, A.A., AbdEldaiem, A.M., 2018. Preparation and characterization of green adsorbent from waste glass and its application for the removal of heavy metals from well water. Adv. Environ. Res. 7 (1), 53–71.
Ray, R.R., 2016. Adverse hematological effects of hexavalent chromium: an overview. Interdiscip. Toxicol. 9 (2), 55–65.
Reddy, S., Jabez Osborne, W., 2020. Heavy metal determination and aquatic toxicity evaluation of textile dyes and effluents using Artemia salina. Biocatal. Agric. Biotechnol. 25, 101574.
Salem, S.S., Fouda, A., 2021. Green synthesis of metallic nanoparticles and their prospective biotechnological applications: an overview. Biol. Trace Elem. Res. 199 (1), 344–370.
Salih, S.S., Mahdi, A., Kadhom, M., Ghosh, T.K., 2019. Competitive adsorption of As (III) and As (V) onto chitosan/diatomaceous earth adsorbent. J. Environ. Chem. Eng. 7 (5), 103407.
Salih, S.S., Mohammed, H.N., Abdullah, G.H., Kadhom, M., Ghosh, T.K., 2020. Simultaneous removal of Cu (II), Cd (II), and industrial dye onto a composite chitosan biosorbent. J. Polym. Environ. 28 (1), 354–365.
Shabani, K.S., Ardejani, F.D., Badii, K., Olya, M.E., 2017. Preparation and characterization of novel nano-mineral for the removal of several heavy metals from aqueous solution: batch and continuous systems. Arab. J. Chem. 10, S3108–S3127.
Shi, Q., Zhang, H., Shahab, A., Zeng, H., Zeng, H., Bacha, A.R., Nabi, I., Siddique, J., Ullah, H., 2021. Efficient performance of magnesium oxide loaded biochar for the significant removal of Pb^{2+} and Cd^{2+} from aqueous solution. Ecotoxicol. Environ. Saf. 221, 112426.
Simeon, E.O., Idomo, K.B.S., Chioma, F., 2019. Physicochemical characteristics of surface water and sediment of Silver River, Southern Ijaw, Bayelsa State, Niger Delta, Nigeria. Am. J. Environ. Sci. Eng. 3 (2), 39–46.
Stidworthy, M.F., Denk, D., 2018. Sphenisciformes, Gaviiformes, Podicipediformes, Procellariiformes, and Pelecaniformes. In Pathology of Wildlife and Zoo Animals (pp. 653–686).
Thiagarajan, S., Sanmugam, A., Vikraman, D., 2017. Facile methodology of sol-gel synthesis for metal oxide nanostructures. Recent Applications in Sol-Gel Synthesis. IntechOpen, pp. 1–17.
Tijani, J.O., Ugochukwu, O., Fadipe, L.A., Bankole, M.T., Abdulkareem, A.S., Roos, W.D., 2019. One-step green synthesis of WO_3 nanoparticles using Spondias mombin aqueous extract: effect of solution pH and calcination temperature. Appl. Phys. A 125 (3), 162–173.
Weerasooriya, R.R., Liyanage, L.P.K., Rathnappriya, R.H.K., Bandara, W.B.M.A.C., Perera, T.A.N.T., Gunarathna, M.H.J.P., Jayasinghe, G.Y., 2021. Industrial water conservation by water footprint and sustainable development goals: a review. Environ. Dev. Sustain. 1–49.
World Health Organization (WHO), 2007. International Drinking Water Standards, third ed. WHO, Geneva.
Xu, C, Shi, S, Wang, X, Zhou, H, Wang, L, Zhu, L., Zhang, G, Xu, D, 2020. Electrospun SiO_2-MgO hybrid fibers for heavy metal removal: characterization and adsorption study of Pb (II) and Cu (II). J. Hazard. Mater. 381, 120974.
Yang, J., Hou, B., Wang, J., Tian, B., Bi, J., Wang, N., Li, X., Huang, X., 2019. Nanomaterials for the removal of heavy metals from wastewater. Nanomaterials 9 (3), 424.
Yaseen, D.A., Scholz, M., 2019. Textile dye wastewater characteristics and constituents of synthetic effluents: a critical review. Int. J. Environ. Sci. Technol. 16 (2), 1193–1226.
Yemmireddy, V.K., Hung, Y.C., 2017. Using photocatalyst metal oxides as antimicrobial surface coatings to ensure food safety-Opportunities and challenges. Compr. Rev. Food Sci. Food Saf. 16 (4), 617–631.
Zhang, Q, Xu, M, Shen, Z, Wei, Q, 2017. A nanostructured Cr_2O_3/WO_3 p–n junction sensor for highly sensitive detection of butanone. J. Mater. Sci.: Mater. Electron. 28 (16), 12056–12062.